GRADUATE COURSE IN PHYSICS
UNIVERSITY OF PISA

The School of Graduate Studies in Basic Sciences "GALILEO GALILEI"

PhD Thesis:

"Coherent algorithm for reconstructing the location of a coalescing binary system using a network of three gravitational interferometers"

Candidate

Simona Birindelli

Supervisor

Andrea Viceré

Al mio babbo

Contents

Introduction

The Virgo project is one of the ground based interferometers on the earth surface that aim to detect gravitational waves. This thesis work concerns the data analysis for the coalescing binaries stars, that are among the most promising gravitational waves sources, since the shape of their signal is well known. The gravitational waves emission from a binary system of compact stars acts like a sort of feedback: the system radiates loosing its orbital energy, so the orbit shrinks and the emission becomes stronger. The signal is therefore called a "chirp", due to this characteristic amplitude and frequency increasing with time. The expectation rate for the double neutron stars merging [32] is $3.4 \cdot 10^{-5}$ per year. Translated in detection expectation rate this corresponds to a detected event every 125 years for the LIGO detectors, and one every 148 years for the Virgo one. For the advanced new generation of detectors, that will be working within the next years, the expectation rate computed by the authors of [32] with the 2004 proposed configuration of advanced detectors is definitely better: 6 events per year for the so called Enhanced LIGO, and 3 every two years [32] for the Advanced Virgo configuration proposed in [38] (updated scenarios for detection rates, with a more recent Advanced Virgo configuration are under development). The technique that suites at best the analysis of this kind of signal is the matched filter, that consists in computing the correlation between the data stream (output of the gravitational waves interferometer) and a set of theoretical templates. From this analysis, using a single detector, it is possible to determine the masses of the two stars, and the so called optimal orientation distance, that is the source distance provided that the orbit has the best inclination with respect to the interferometer line of sight. Reconstructing the source position, so as to draw a gravitational waves sources sky map, requires at least three non-coincident detectors, in order to make a triangulation. Another very good reason to use a network of gravitational waves interferometers is that the detection rate can be improved considering a network of three detectors (Virgo, Hanford and Livingston) and operating a coherent analysis as described in [1] , since in this case the expected rate corresponds to one event each 26 years [32]. There are two different methods used for the network analysis: the coincident method, and the coherent one. The first is the most intuitive one, and simply consists in a separate single detector analysis performed by each interferometer, and a successive comparison between the single detector candidates, searching for compatible events. After that process, only the coincidences remain as candidate events, and they can be used for the source position

reconstruction, using the time delays between detectors. The basic idea of the coherent method is to "construct" an ideal detector equivalent to the network, to which each real interferometer coherently contributes with its sensitivity, location, orientation. For this purpose a so called network statistic to maximize in order to extrapolate the source parameters is constructed, first, and maximized then [1]. For this thesis we have worked on coalescing binaries network analysis, trying to determine the best strategy for source position reconstruction. We have developed a pipeline that implements a fully coherent method, in a few different variations, and we have compared them with the classical time-of-flight coincidence analysis. The coincident method has been optimized in order to make a fair comparison; in particular we have adopted the reference time [31], for implementing the coincidence, and we have further improved the arrival time accuracy by fitting the shape of the matched filter response. Among the coherent techniques tested, the simplest has been a direct maximization of the network likelihood. A fit of the likelihood to improve the determination of the likelihood maximum has also been attempted but the fitting procedure resulted unstable; instead, we have found most effective to define the most likely declination and right ascension by means of an average procedure weighted by the corresponding network likelihood. This procedure allows to remove the discretization effect due to the finite sampling rate of the analysis, and provides results compatible with the ones obtained with the time-of-flight technique, and in a relatively automatic way.

The study of the accuracy problem, comparing the two methods of analysis gives in a certain way two important consequences: first of all the determination of the best coherent strategy for reconstructing the source position among all the alternatives, both in terms of efficiency, and in term of computational costs; and as a secondary effect it gives us the incipit for push the coincident method to its best, provided that one uses all the correlators information.

If we give a glance to the future, since new interferometric gravitational waves detectors are under construction and under project, another important feature of the coherent method is its flexibility to be adapted to a larger number of detectors. The coherent method can tell us how to combine them in order to obtain with the best accuracy the source position, instead of analyzing all the possible independent triangulations, and loosing in that way part of the event astrophysical information.

Part I

From Einstein equations to gravitational waves interferometers

Chapter 1

Einstein equations and gravitational waves...

The basic idea of the General Relativity theory is that matter and energy determine space-time curvature. Einstein equations allow us to characterize the relationship between the "shape" of space-time and its matter and energy distribution. This so tricky connection is embedded in a set of 10 differential equations for the space-time metric, that are non-linear and mutually dependent:

$$\mathbf{G} = 8\pi\mathbf{T} \tag{1.1}$$

where $\mathbf{G}$ is the so called "Einstein tensor", which is a symmetric 2-dimensional tensor, constructed starting from the Riemann tensor, a 4-dimensional tensor function of second derivatives of the metric, it completely characterize the space-time curvature. $\mathbf{T}$ is the stress-energy tensor, which describes the distribution of matter and energy in the considered Universe.

Due to their complicated form, most of the solutions of Einstein equations are obtained numerically.

In the empty space, namely far enough from a mass distribution so that one could approximately consider a flat space-time (neglecting the possible Universe cosmological curvature), it is possible to linearize Einstein equations and consider the mass effects such as perturbations in a minkowskian flat space-time:

$$g_{\alpha\beta} = \eta_{\alpha\beta} + h_{\alpha\beta} \qquad |h_{\alpha\beta}| \ll 1 \tag{1.2}$$

By choosing the so called Lorentz gauge (which fixes 4 of the 10 independent elements of $h_{\alpha\beta}$) the linearized Einstein equations in the empty space assume the form:

$$\Box h_{\alpha\beta} = 0 \tag{1.3}$$

which remind one of Maxwell equations. To these equations can be applied the so called traceless transverse (TT) gauge, that fixes another 4 of the 6 independent components

of the metric tensor. Like Maxwell equations, these linearizations have a plane waves solution:

$$h_{\alpha\beta} = a_{\alpha\beta}\, e^{(ik_\lambda x^\lambda)} \tag{1.4}$$

$a_{\alpha\beta}$ are complex constants that can be expressed in a very simple way thanks to the TT gauge:

$$a_+ = A \begin{pmatrix} 0 & 0 & 0 & 0 \\ 0 & 1 & 0 & 0 \\ 0 & 0 & -1 & 0 \\ 0 & 0 & 0 & 0 \end{pmatrix} \quad a_\times = A \begin{pmatrix} 0 & 0 & 0 & 0 \\ 0 & 0 & 1 & 0 \\ 0 & 1 & 0 & 0 \\ 0 & 0 & 0 & 0 \end{pmatrix} \tag{1.5}$$

Thus these solutions are monochromatic plane waves with two different polarizations. The null time elements of the matrices suggest that the waves travel through space, at the speed of light.

The constant A represents the wave amplitude, and is related to the source features (see chapter 2).

The two polarizations have a 45° relative phase displacement, and this peculiarity gives a different observational effect over two orthogonal directions, as better explained in paragraph 1.1. From the quantistic point of view, one can say that as for the electromagnetic waves, where the two polarization states correspond to photons that carry one angular momentum unity ($\pm\hbar$), one has that the quantization of the weak gravitational field leads to "gravitons" that transport two angular momentum unity (due to the relative phase displacement value)[7].

1.1 Order of magnitude of gravitational waves amplitude

In order to have an idea of the amplitude of a gravitational wave, it is interesting to make a comparison between electromagnetic and gravitational radiation. The expression for an electromagnetic field coming from any charge distribution, truncated to its first terms of a multipole expansion, is:

$$\overrightarrow{E} = \frac{1}{c^2 r}\left[\left(\ddot{\overrightarrow{p}} \times \hat{n}\right) \times \hat{n} + \hat{n} \times \ddot{\overrightarrow{\mu}} + \left(\dddot{\overrightarrow{q}} \times \hat{n}\right) \times \hat{n}\right] + ... \tag{1.6}$$

where r is the distance between source and observer, and $\hat{n}$ the unitary vector towards the r direction. The formula contains the first terms of a multipole expansion: the electric dipole $\overrightarrow{p} = \sum_a e_a \overrightarrow{r_a}$,the magnetic dipole $\overrightarrow{\mu} = \frac{1}{2c} \sum_a e_a \overrightarrow{r_a} \times \overrightarrow{v_a}$, and $\overrightarrow{q}$ that is a function of the electric quadrupole Q^{ij}.

The corresponding electromagnetic luminosity results:

$$L_{em} = \frac{2}{3c^3} \left| \ddot{\overrightarrow{p}} \right|^2 + \frac{2}{3c^3} \left| \ddot{\overrightarrow{\mu}} \right|^2 + \frac{1}{20c^5} \dddot{Q}^{ij} \dddot{Q}_{ij} \tag{1.7}$$

One can compute the corresponding quantities for the gravitational radiation:

$$\overrightarrow{p} = \sum_a m_a \overrightarrow{r_a} \tag{1.8}$$

form which one can see that $\ddot{\overrightarrow{p}} = 0$ because of the momentum conservation. In the same way one has the equivalent of the magnetic dipole:

$$\overrightarrow{\mu} = \frac{1}{2c} \sum_a m_a \overrightarrow{r_a} \times \overrightarrow{v_a} \tag{1.9}$$

and from the angular momentum conservation $\dot{\overrightarrow{\mu}} = 0$.

Thus the first non-zero term is the quadrupole one, defined as: $Q^{ij} = \sum_a m_a \left(x_a^i x_a^j - \frac{1}{3} r_a^2 \delta^{ij} \right)$, that is the traceless part of the moment of inertia tensor. So the gravitational luminosity assumes the form:

$$L_{grav} = \frac{G}{5c^5} \left\langle \dddot{Q}^{ij} \dddot{Q}_{ij} \right\rangle \tag{1.10}$$

It is interesting to notice that

$$\frac{5c^5}{G} = 3.6 \cdot 10^{59} erg\ s^{-1} \tag{1.11}$$

to be compared with the solar luminosity $L_\odot = 3.8 \cdot 10^{33} erg\ s^{-1}$.

For example if one has a mass distribution moving periodically with period T, such as a stellar binary system, $Q \sim M_{tot} R^2$ where R is the orbital radius, it follows that $\dddot{Q} \sim \frac{M_{tot} R^2}{T^3} \sim \frac{E_{kin}}{T} = L_{int}$, where the internal luminosity is the power of the internal energy transfer, so finally

$$L_{grav} \sim L_{int}^2 \tag{1.12}$$

The system is gravitationally bound, so its kinetic energy has the same order of magnitude of the potential energy, which can be approximated by $\frac{M_{tot}^2}{R}$. Using the third Kepler law ($R^3 \sim M_{tot}T^2$), and geometrized unit system, one has that

$$L_{grav} \sim \left(\frac{M_{tot}}{R}\right)^5 \tag{1.13}$$

In this unit system a mass is "represented" by its Schwartzschild radius[1], so if one has an one solar masses twin binary system with an Astronomical Unit ($149.6 \cdot 10^9 m$) orbital radius $L_{grav} \simeq (10^{-8})^5 = 10^{-40} = 10^{-19} ergs^{-1}$that is very faint. But as the "compactness" reaches 10^{-5} the luminosity increases $L_{grav} \simeq 10 L_\odot$[7].

[1]The Schwartzschild radius of a given mass is the quantity $R_S = \frac{2Gm}{c^2}$ It is useful to determine the compactness of a stellar object: normally the ratio $\frac{R_S}{R} \ll 1$, and it increases as the object become more compact. When an object reaches the dimension of its Schwartzschild radius becomes a black hole.

Chapter 2

Brief summary of gravitational waves sources

From the previous section we know that observational effect of a gravitational waves can be detected only if the source is an astrophysical object. Indeed the main features of a good gravitational waves source is to be an accelerating object with a huge mass. Translated in the language of astrophysics, this sounds like "compact star with a non-zero third time-derivative of gravitational quadrupole".

Among the astrophysical processes and objects with this kind of features we find non-spherical supernovae explosions, not-perfectly spherical pulsars, the coalescence of compact binary systems, and the cosmological radiation after the Big Bang.

2.1 The birth of stars and binary systems

About half of the catalogued stars belong to a binary system, a configuration supported by stars formation processes. The stars formation regions, the so called molecular clouds, are made up of interstellar dust that starts to collapse searching for its stable configuration. The collapse stops when the scattering between dust particles starts to contrast the gravitational energy of the cloud. In this stage of cloud evolution some auto-gravitating cloud fragments with density $10^2 - 10^3 g \cdot cm^{-3}$ begin to form, they are the so called protostars.

In absence of rotation the fragments would tend to reach a spherical shape, but in most cases the molecular cloud had a nonzero angular momentum, that had been shared among the protostars by the fragmentation process. The stable configuration of a slightly rotating fluid is a bi-axial ellipsoid [14]. As the ratio between rotation and gravitational energy increases, the stable shape rises the so called Mc Laurin sequence, as far as the new stable configuration becomes a tri-axial ellipsoid, more and more distorted as the rotation increases (Jacobi's sequence). These distortions lead easily to an "handlebars" structure, progenitor of a binary system [14].

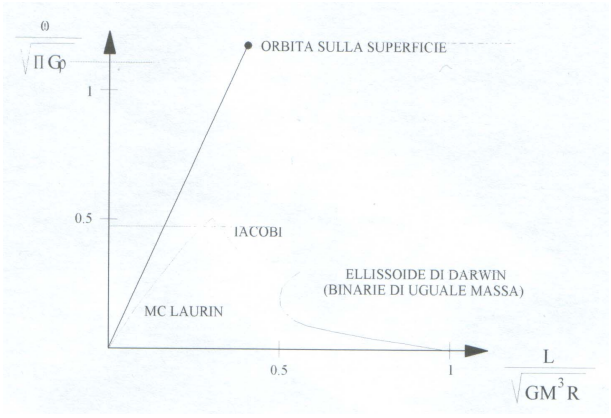

Figure 2.1:
The Mc-Laurin curve, showing the shape of the protostar as a function of its binding energy

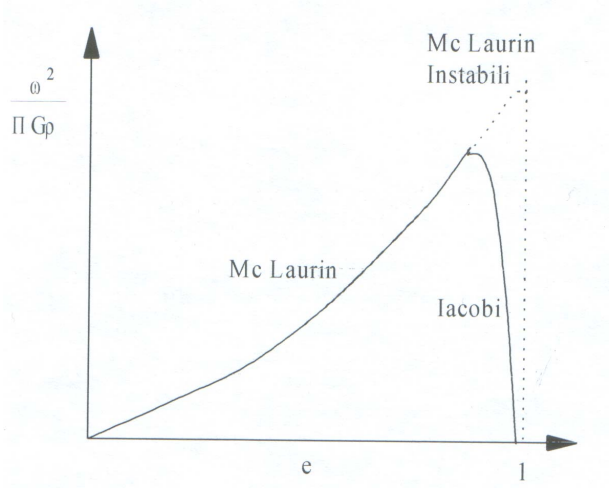

Figure 2.2:
The so called Mc Laurin-Jacobi sequence, showing the point of instability of a single protostar, and the birth of a binary system

From the molecular cloud collapse and fragmentation a proto-stellar cluster is born. At this moment the cloud will evolve in order to reach the thermodynamic equilibrium as "gas of stars", and it will reach the stable configuration from "open" to "globular" cluster. During this period the interaction between stars will be very important, since they can help the formation of new binary systems, or tends to substantially modify existing ones. Each single cloud component, both single protostar or proto-binary system, will evolve according to the stellar evolution processes.

2.2 A brief look at stellar evolution: transformations and processes of a star from birth to death.

Focusing on a single proto-star, we will briefly summarize its life in a very simplified way.

First of all, the proto-star begins to collapse towards the stability, and it will reach its equilibrium with the primer of nuclear reactions. As far as these reactions can completely guarantee the hydrostatic and energetic equilibrium of the object, the newborn star can

be inserted by the astrophysicists in the so called Hertzsprung-Russel (H-R) diagram. The diagram shows the stars luminosity as a function of their temperature, and one can in principle follow the life of a star through its "movements" inside the diagram, but since the human mean lifetime is much shorter compared with a star mean lifetime, one can "only" determine the ages of the existing stars, and reconstruct their evolution.

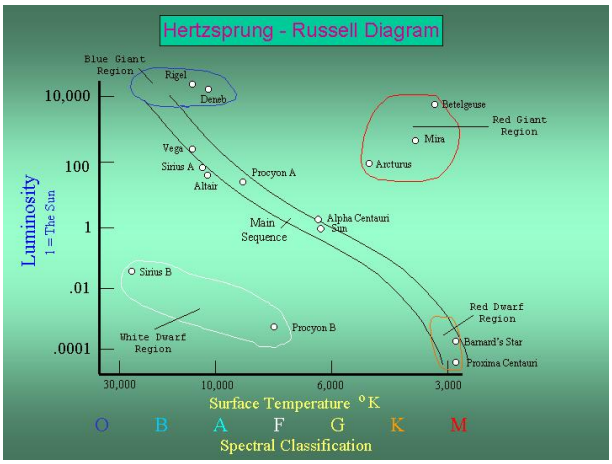

Figure 2.3: An explicative picture of the H-R diagram, taken from http://astroimage.homestead.com/StellarEvolution3.html

The life of a star depends predominantly on its mass [15]. The first significant distinction appears with the "ignition" of the hydrogen fusion, since the low mass stars (up to $1.2\,M_{\odot}$, inferior part of the Main Sequence in a H-R diagram) burn through the "p-p" reaction into the radiative core, and have an inert convective envelop; the high mass stars reach higher inner temperatures, that renders the core convective, and favores the CNO reaction, which uses the three heavier elements as catalysts (superior part of the main Sequence in a H-R diagram).

As the hydrogen core is totally burned, the fusion starts in the outer layers, and the released energy constrains the star to expand itself up to 10 times its original dimension searching for stability (Red Giant phase in a H-R diagram). After this phase the star has to contract itself so as to begin the helium core fusion, if its mass is at least $0.5\,M_{\odot}$, if not the contraction will lead the star nuclear matter to degenerate ($\rho \approx 10^{6} g\,cm^{-3}$) unil the electron gas pressure balances the gravitation energy, when the star reaches its stability and becomes a white dwarf.

The succession of expansion and contraction, burning heavier elements as it goes on, continues in the stars able to burn helium, while the mass constrains proceed with their selection at every step, creating some more white dwarfs (at the first step) and supernovae explosions. More in details, when a star has to contract its helium (or heavier element) core in order to start the next fusion, the contraction makes the nuclear matter to degenerate, and the burning starts with an explosion that ejects the external layers of the star. The explosion reach enormous luminosities, up to $10^{10} L_{\odot}$(supernova). If the burning core is carbon, the star will blow out as an oxygen-neon white dwarf.

Higher masses stars peacefully reach an iron-nichel core, at this point the fusion becomes disfavored from the energetic point of view, and the star can only contract itself searching for an equilibrium. So the nuclear matter becomes degenerate, and since the core mass exceeds the Chandrasekhar limit for a gas of degenerate electrons ($1.44\,M_\odot$) the collapse does not stop. Pressure and temperature conditions make energetically favored the $\beta - inverse$ reaction $p + e^- \rightarrow n + \nu_e$, which launches the so called neutronization process. Meanwhile in the inner part of the core, that collapses with sub-sonic speed, the primer of some reactions in a degenerate environment originates a shock wave. When the shock wave reaches the outer core, that collapses with a super-sonic speed in a dishomogeneus way, the results is a powerful explosion that throws out the external layers of the star. After the explosion the survivor core is completely neutronized, and depending on its initial mass, the destiny of the star is to become a neutron star or a black hole. If the progenitor mass was in the range $8 \div 20\,M_\odot$the supernova remnant, a degenerate neutron gas, is able to become an extremely dense and compact auto-gravitating object: a neutron star is born ($\rho \simeq 10^9 g\,cm^{-3}$, $R \simeq 10\,km$).

Primogenitors heavier than $20\,M_\odot$ can only collapse to a black hole, in different ways depending on the mass. Here it is a very brief summary:

$20\,M_\odot < M < 42\,M_\odot$ or $48\,M_\odot < M < 72,3\,M_\odot$ supernova explosion with remnant core collapsing directly to a black hole;

$42\,M_\odot < M < 48\,M_\odot$ or $M > 72,3\,M_\odot$ direct collapse to a black hole when the reactions extinguish, without supernova explosion (external layers fall immediately into the core) [4].

Stars with masses above in the range $48\,M_\odot < M < 72,3\,M_\odot$ have a peculiarity: they have a very high loosing mass rate, increasing with the star mass, so they acts as lighter stars, and experiences a supernova explosion despite of their masses would suggest.

2.3 Supernovae explosions

The supernovae explosions represent the last stage of massive stars life (see paragraph 2.2). Astrophysicists distinguish two different kind of supernova explosions, depending on processes that generate them.

Type Ia supernovae originate from binary systems where a component is a white dwarf. If the orbit is tight enough a mass transfer starts from the companion to the dwarf. Accreting its mass, the white dwarf exceeds its Chandrasekhar mass limit[1] and starts to collapse. Due to the contraction nuclear reactions violently start releasing such a big amount of energy to make the star explode. Their spectra present no hydrogen lines, but a singly-ionized silicon (Si II) line at 615.0 nm.

Type Ib spectra present non-ionized helium (He I) line at 587.6 nm and no strong silicon absorption feature near 615 nm, they are supposed to originate from massive stars

[1]The Chandrasekhar limit is the maximum non-rotating mass which can be supported by an auto-gravitating gas of degenerate electrons. Its value is 1.44 solar masses.

that lose their mass rapidly by a very strong stellar wind (just to make a comparison, the Sun loses $10^{-16} M_{\odot}$ per year, this kind of star loses $10^{-5} M_{\odot}$ per year).

Type Ic spectra present weak or no helium lines and no strong silicon absorption feature near 615 nm, and they originate from the collapse of a massive stars.

Type II supernovae are the death of massive stars that end their nuclear fuel and begin to contract searching for their stable configuration. At a certain point, the contraction generates a shock wave that propagate form the inner core to the external layers, and ejects them with an explosion. The collapse releases an enormous amount of energy, at least equal to the binding energy of a neutron star, about $0.15\, M_{\odot} c^2$[17]. Most of this energy is carried away by neutrinos. The amount of energy released by gravitational waves is the energy flux F[17]:

$$F = \frac{c^3}{16\pi G} \left| \dot{h} \right|^2 \tag{2.1}$$

where h is the gravitational wave amplitude. If the source is at a distance r from the detector, and if the waves carry a total energy E emitted at a frequency f_{gw} for a period T , the amplitude h will be:

$$h = 5 \times 10^{-22} \left[\frac{E}{10^{-3} M_{\odot} c^2} \right]^{1/2} \left[\frac{T}{1\, ms} \right]^{-1/2} \left[\frac{f_{gw}}{1\, kHz} \right]^{-1} \left[\frac{r}{15\, Mpc} \right]^{-1} \tag{2.2}$$

The equation shows that a burst emitting $10^{-3}\, M_{\odot}$ in gravitational-wave energy (less than 1% of the available energy), at the distance of the Virgo Cluster (18 Mpc), would have an amplitude that is comparable with the sensitivity of the first generation of ground-based interferometers like Virgo and the LIGOs , provided its energy comes out around 300 Hz [17].

F. Mannucci, D. Maoz, K. Sharon, M. T. Botticella, M. Della Valle, A. Gal-Yam and N. Panagia [33] computed the supernovae expected rates in the Local Universe for each type of supernova.

Type	Ngal	Ia		Ib/c		II		CC	
		N	Rate	N	Rate	N	Rate	N	Rate
					Cluster $D < 0.5$ Mpc				
E/S0	430	11.0	$0.066^{+0.027}_{-0.020}$	0.0	< 0.020	0.0	< 0.027	0.0	< 0.047
S0a/b	251	1.5	$0.031^{+0.052}_{-0.023}$	2.5	$0.094^{+0.105}_{-0.056}$	1.0	$0.056^{+0.131}_{-0.049}$	3.5	$0.150^{+0.132}_{-0.077}$
Sbc/d	100	0.0	< 0.34	0.0	< 0.64	3.0	$1.37^{+1.34}_{-0.76}$	3.0	$1.376^{+1.347}_{-0.761}$
Irr	29	0.0	< 5.4	0.0	< 7.3	1.0	$5.79^{+13.4}_{-5.01}$	1.0	$5.79^{+13.4}_{-5.01}$
TOT	810	12.5	$0.057^{+0.021}_{-0.016}$	2.5	$0.020^{+0.022}_{-0.012}$	5.0	$0.057^{+0.039}_{-0.025}$	7.5	$0.077^{+0.040}_{-0.028}$
					Cluster $D < 1.5$ Mpc				
E/S0	723	15.0	$0.058^{+0.019}_{-0.015}$	0.0	< 0.012	0.0	< 0.017	0.0	< 0.029
S0a/b	519	4.8	$0.048^{+0.034}_{-0.021}$	2.7	$0.044^{+0.047}_{-0.026}$	2.5	$0.061^{+0.068}_{-0.036}$	5.2	$0.104^{+0.069}_{-0.045}$
Sbc/d	321	4.8	$0.152^{+0.105}_{-0.067}$	0.6	$0.031^{+0.105}_{-0.031}$	8.5	$0.610^{+0.290}_{-0.206}$	9.1	$0.641^{+0.290}_{-0.209}$
Irr	94	3.0	$1.82^{+1.78}_{-1.00}$	1.0	$1.28^{+2.96}_{-1.10}$	1.0	$1.67^{+3.88}_{-1.45}$	2.0	$2.94^{+3.91}_{-1.94}$
TOT	1666	27.7	$0.070^{+0.016}_{-0.013}$	4.3	$0.018^{+0.014}_{-0.008}$	12.0	$0.072^{+0.028}_{-0.021}$	16.3	$0.090^{+0.028}_{-0.022}$
					Field				
E/S0	1326	5.0	$0.019^{+0.013}_{-0.008}$	0.0	< 0.015	0.0	< 0.020	0.0	< 0.034
S0a/b	2393	15.7	$0.059^{+0.019}_{-0.015}$	3.3	$0.026^{+0.023}_{-0.014}$	12.0	$0.130^{+0.049}_{-0.037}$	15.3	$0.155^{+0.051}_{-0.039}$
Sbc/d	2362	15.8	$0.140^{+0.045}_{-0.035}$	5.8	$0.121^{+0.075}_{-0.049}$	23.5	$0.652^{+0.164}_{-0.134}$	29.2	$0.773^{+0.171}_{-0.142}$
Irr	551	3.3	$0.426^{+0.38}_{-0.22}$	1.1	$0.300^{+0.62}_{-0.25}$	4.5	$1.47^{+1.08}_{-0.67}$	5.7	$1.77^{+1.11}_{-0.73}$
TOT	6683	39.8	$0.061^{+0.011}_{-0.010}$	10.2	$0.033^{+0.014}_{-0.010}$	40.0	$0.174^{+0.032}_{-0.027}$	50.2	$0.207^{+0.034}_{-0.029}$

Figure 2.4:
The table summarizes the results obtained by F. Mannucci, D. Maoz, K. Sharon, M. T. Botticella, M. Della Valle, A. Gal-Yam and N. Panagia [33] while computing the supernovae expected rates in the Local Universe, for each type of supernova.

where in the first column are the galaxy types, in the second the number of galaxies, then there are shown, for each supernova type, the number of supernovae and the supernovae rate measured in SNuM (supernovae per century per $10^{10} M_{\odot}$ of stellar mass). In the CC (core collapse) columns, the sum of the type Ib/c and II results are reported.

An additional help to gravitational waves detectors would be a coincidence with an electromagnetic or neutrinos supernova detection.

2.4 Pulsars

Compact stars, like "simple" neutron stars or pulsars radiate gravitational waves due to their rotational motion, provided that they are significantly non-axisymmetric. The non-axisymmetries may come from irregularities in the crust, formed when, after the collapse, the spin velocity was strongly increased due to the angular momentum conservation, and they could be frozen in as the star cooled. The shape of the crust may depend also on the star quakes, and the gravitational radiation can belongs to the star history too: due to a violent formation, such as a supernova explosion, or to its environment such as an accretion disk from a giant companion, the rotation axis may not coincide with the principal axis of the star moment of inertia, and it may cause the star to precess and consequently, to radiate gravitational waves [24]. A different kind of non-axisymmetries can be due to the excitation of normal modes of pulsation, or to the precession that can

occur after the accretion of the stellar spin [17].

Regarding the pulsars, a source of non-axisymmetry is the off-axis magnetic field of the star, it can produce Lorentz forces on the conducting (or superconducting, as supposed by Bonazzola and Gourgoulhon) matter that can distort the star shape, and make it gravitationally radiate [24]. If one calls α the angle between rotation and distortion axes, one has that for aligned axes ($\alpha = 0, \pi$) the gravitational radiation is null, if they are perpendicular ($\alpha = \pi/2$) the stars emits gravitational waves at twice the rotation frequency, in all the intermediate cases, the gravitational emission has two frequencies, the rotational ones and twice it. For small values of α, that is for not-so-misaligned axes, the emission at the lower frequency dominates [24].

Assuming that the derivative of the rotational period $\dot{T}$ is related to the magnetic dipole moment of the star, the gravitational waves emission can be described in terms of two observable parameters T and $\dot{T}$, and of a third parameter, β which measures the distortion response of the star to a given dipole magnetic moment, and it depends on the neutron stars matter equation of state, and on the star magnetic field distribution. The gravitational waves amplitude at the higher frequency does not depend on the inclination of the distortion axes with respect to the rotation axes α, as for the emission at lower frequency the amplitude increases as α decreases.

In order to have an idea of the gravitational radiation emitted by a pulsar, one can use a sort of "toy model", considering a $1.4\,M_{\odot}$neutron star with 10 km radius, moment of inertia $I = 10^{38} kg\,m^2$ and rotational frequency ν. The order of magnitude of the emitting gravitational wave will be of order[17]

$$h \sim \frac{4\pi^2 G}{R\,c^4} \epsilon\, I\, \nu^2 \tag{2.3}$$

As one can see the energy loss rate is also related to the star ellipticity $\epsilon = 1 - \frac{b}{a}$ where a is the semi-major axis of the equatorial section and b the semi-minor ones. The ellipticity of a neutron star is related to its rotating period and its rate of change [17]:

$$\epsilon = 5.7 \times 10^{-3} \left(\frac{T}{1\,s}\right)^{3/2} \left(\frac{\dot{T}}{10^{-15}}\right)^{1/2} \tag{2.4}$$

Assuming that the spin-down is entirely due to the gravitational waves emission, for the Crab the formula gives $\epsilon = 7 \times 10^{-4}$, the real ellipticity (considering all the mechanism that can contribute to the spin-down) might be a factor 100 below this. Pulsar J0437-418 is the nearest millisecond pulsar, and its ellipticity would have to be only about 10^{-8} to produce radiation at an amplitude that the ground base interferometers could detect if the interferometer response is tuned to be resonant at the expected GW frequency (the so called " narrow-banding" method).

Using the total spin-down to place an upper limit on h, Schutz [17] has found that the

upper limits on the gravitational radiation from the Crab and Vela pulsars is of the order of 10^{-24}.

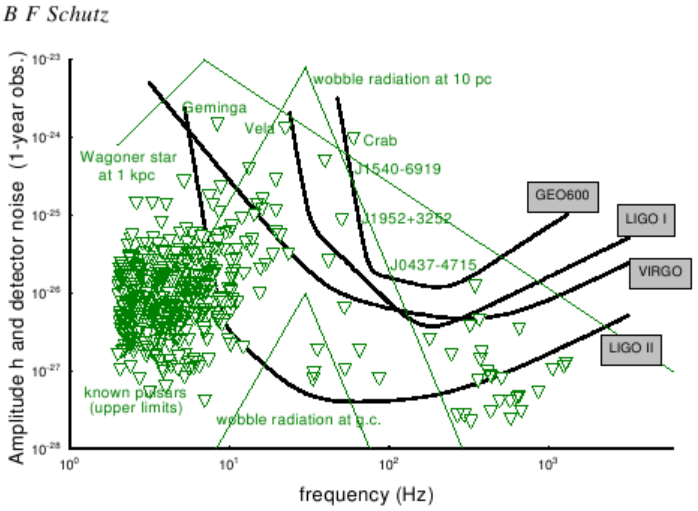

Figure 2.5:
The plot [17] shows the upper limits on h for all the pulsars emitting gravitational waves at a frequency above 7 Hz and whose spin-down rate has been measured.

Very rapidly rotating neutron stars can have unstable normal modes caused by the CFS instability [2]. These modes are present when rotation rates reach about 1 kHz (depending on the equation of state), but the mode frequencies seem to be low, of the order of a few hundred Hz. The emission grows until it has radiated away enough angular momentum from the star to reduce its spin below the instability point. The amplitudes of these modes could be large enough to make them detectable from the Virgo Cluster even by first-stage interferometric detectors. The radiation duration is a few seconds, but the observational time can be very long, months, or years, so that to improve the detection probability. If one knows the structure of the waveform the effective sensitivity can be achieved using the matched filtering procedure, obtaining an improvement of roughly $h\sqrt{n}$, where n is the number of cycles in the waveform, proportional to the integration time T: $n = T\, f_{gw}$.

2.5 Stochastic background

Soon after the Big Bang there was a thermal equilibrium between all the elementary particles due to their interactions. The primordial "fireball" progressively became cooler

[2] At rotation rates slightly below the ones that deform the star into a bar shape ($E_{kin}/U_{grav} \sim 0.27$ in the case of Mc Laurin spheroids) a star can become unstable to secular non-axisimmetric instabilities, due both to gravitational radiation and viscosity. These instabilities appears when a mode that is retrograde in a star co-rotating frame, appears as pro-grade to a distant inertial observer, through the Chandrasekhar-Friedman-Schutz (CFS) mechanism: a mode that is retrograde in the co-rotating frame has negative angular momentum, since the perturbed star has less angular momentum than the unperturbed one. If, for an inertial distant observer, the mode is pro-grade, it removes positive angular momentum from the star, so the angular momentum of the mode increases negatively.

The instability evolves on a secular timescale, during which the star loses angular momentum via gravitational waves. When the spin reaches a lower threshold, the mode becomes stable [24].

because of its expansion, and particles started to decouple. Since the gravitons are the only particles that gravitationally interact only, they decoupled first, and the gravitational waves emission starts. This is an important difference from the microwaves background, which was thermalized and strongly coupled to matter until the epoch of recombination. So, while the microwaves electromagnetic radiation comes from about $3 \cdot 10^5$ years after the Big Bang, the gravitational radiation comes from a much earlier time, more or less only 10^{-44} seconds after the explosion [25]. This radiation is therefore primordial, and apart from a cosmological redshift it is unchanged since it was produced, so this is a very important "picture" of the Universe at age 10^{-44} seconds. Also with the microwaves background one can extract information about the Universe at earlier times then the photon decoupling, but, quoting M. Maggiore, it would be like "trying to understand the aspect that a person had as a child from a picture taken when he was much older", and gravitational waves can strongly improve, since they "provide directly a picture of the child, and therefore give us really unique information" [25].

Besides the emission produced by the cosmological background, the superposition of a large number of unresolved sources at high redshifts will produce a gravitational waves stochastic background. They can be divided into three different kind of signals: the continuous background, to which are supposed to contribute tri-axial rotating neutron stars, magnetars and the final stage of the coalescence of double neutron stars for sources beyond $z \sim 0.5$ [26]; the so called "popcorn" intermediate noise, coming from supernovae, hypernovae and coalescing neutron stars with $0.2 < z < 0.5$ [26]; and the shot noise, reasonably produced by distorted black holes, bar mode emission from young neutron stars, and coalescing binaries nearer than $z \sim 0.2$ [27].

The radiation consists of many individual components superimposed in a random way. It can be described using its energy density as a function of frequency; in order to obtain a dimensionless quantity the spectral energy density $\rho_{gw}(\nu)$ is normalized to the energy density that is required to close the Universe ρ_c

$$\Omega_{gw}(\nu) = \frac{\nu}{\rho_c} \frac{d\rho_{gw}(\nu)}{d\nu} \tag{2.5}$$

where $\rho_c = 2 \times 10^{-43}\, J\, m^{-3}$ with an Hubble constant of $100\, km\, s^{-1}\, Mpc^{-1}$. The radiation is produced by very different kinds of physical processes, so it has no natural length scale. For such a kind of radiation the energy density Ω_{gw} will be independent of frequency. Other kinds of stochastic background models suggest a spectrum whose energy is independent of frequency, so as to have $\Omega_{gw} \propto \nu^3$, and this favors ground based detectors [17].

Such a kind of gravitational waves appears in a detector as one of the several sources of noise. For a single ground based interferometer the expected gravitational waves noise level is so low that it will not be seen against expected instrumental noise sources. But

using two detectors one can cross correlate their output data stream integrating over the observational time. Since the instrumental noise is assumed to be independent in each interferometer, it can be canceled out, while the gravitational wave noise, being the same in both detectors, sums systematically. If the two interferometers were close enough each other to respond in the same way to a given component of the stochastic gravitational wave field, the method would work perfectly. Actually detectors are separated by significant distances (the two LIGOs are about 3000 km far one to each other), and this causes their mutual response to a gravitational wave to de-correlate somewhat. On the other hand, a good correlation detection can be done only if the two instrumental noises are independent, so one has to locate the two interferometers far enough that any seismic vibration noise (for instance) does not correlate between them.

Searching for a stochastic background means searching for a noisy background against the instrumental noise, so the interferometer sensitivity to this kind of signal grows more slowly with respect to a well known coherent signal (for example a periodic signal or a coalescing binaries one), increasing with the observational time as $T_{obs}^{1/4}$. So, if $\Delta\nu$ is the bandwidth of the correlation experiment, the minimum detectable h signal is

$$h_{sto} = \frac{\sigma}{(\Delta\nu T_{obs})^{1/4}} \tag{2.6}$$

where σ is the RMS noise in a single detector over the same bandwidth. If the two detectors are not identical it has to be replaced by the geometric mean of the two different values of σ. If one has bandwidths of 1 kHz and observation times of 10^7 s, this means an improvement of about two orders of magnitude in energy density sensitivity, that correspond to roughly a factor three in amplitude sensitivity, over the sensitivity of a single interferometer.

In order to have an estimate of the order of magnitude of the energy density of a stochastic background signal, one can use the formula:

$$\rho_E = \frac{c^2}{16\pi G}\left|\dot{h}\right|^2 \tag{2.7}$$

For a signal with amplitude of 10^{-22} the energy density divided by the closure density is 10^{-4} . A cross-correlation experiment will improve this limit by five order of magnitude, so it should be able to detect a stochastic background with an energy density as small as 10^{-9} of the closure density [17].

Chapter 3

Gravitational wave detection: the Virgo interferometer

3.1 Observational effects of gravitational waves

A gravitational wave is a particular space-time curvature, so one can calculate its Riemann tensor and see its effect as it passes through the matter. Thanks to the TT gauge, the Riemann tensor has few non-null components:

$$R^i_{0k0} = \frac{1}{2}\ddot{h_{ik}} \tag{3.1}$$

where i, k represent the spatial coordinates, the 0^{th} component is the temporal one.

If two free masses are in a local inertial frame, the passage of a gravitational wave makes the masses oscillate with the tidal acceleration:

$$\frac{d^2 r^i}{dt^2} = -R^i_{0k0} r^k = -\frac{1}{2}\ddot{h_{ik}} r^k \tag{3.2}$$

Since $|h_{ik}| \ll 1$, the oscillation amplitude is supposed to be smaller with respect to the relative distance r_{start}, so the equation becomes:

$$\frac{d^2 \delta r^i}{dt^2} = -\frac{1}{2}\ddot{h_{ik}} r^k_{start} \tag{3.3}$$

After an integration, one obtains:

$$\delta r^i = -\frac{1}{2} h_{ik} r^k_{start} \tag{3.4}$$

which tells one that $\frac{\delta r}{r} \sim h$.

If a spring connects the two masses, there is an additional term in the equation:

$$\frac{d^2\delta r^i}{dt^2} = -\frac{1}{2}\ddot{h_{ik}} r^k_{start} - \omega_0^2 \delta r^i \tag{3.5}$$

and if the gravitational wave is monochromatic with frequency ω, the displacement from the equilibrium is:

$$\delta r^i = \frac{\omega^2 h_{ik}}{2\left(\omega_0^2 - \omega^2\right)} r^k_{start} \tag{3.6}$$

in this case the difference with respect to the free masses is the resonance factor $\frac{\omega^2}{\left(\omega_0^2 - \omega^2\right)}$ that amplifies the signal near to the resonance frequency ω_0.

These two examples are the basic ideas for the two different kind of gravitational waves detectors: the interferometric antennas and the resonant bars [7].

3.2 The basic idea of a gravitational waves interferometer

To start a gravitational waves astronomy is among the most important astrophysical challenges of the XXI century. To this purpose, a network of gravitational waves interferometers has been developed and now it is operating. The network is composed by the Italian-French 3 km arms Virgo, located in Cascina (Pisa, Italy), the three United States LIGOs, one located in Louisiana, at Livingston, with 4 km arms, the other two (the smaller with 2 km arms, the larger with 4 km ones) located at Hanford (Washington), the German-British GEO, a 600 m arms interferometer located at Hannover, and TAMA, a Japanese 300 m arms interferometer.

A gravitational waves interferometer is a Michelson interferometer advisably modified, indeed we have seen (see paragraph 1.1) how faint is a gravitational wave signal, so the most accurate method to detect it has to be used.

Due to the tiny displacement between the two geodetics, that is proportional to the h-amplitude, the initial displacement has to be very large in order to amplify the signal.

The basic idea of the detection method will be briefly explained.

Assuming a flat space, the equation for a geodetic of a light beam is

$$ds^2 = 0 \tag{3.7}$$

If one defines the "detector reference frame" to originate in the Michelson half-reflective mirror, and with axes x and y along the arms, the geodesic for each laser beam will have

the form:

$$0 = ds^2 = (\eta_{\mu\nu} + h_{\mu\nu})dx^\mu dx^\nu = c^2dt^2 - (1 + h_{11})dx^2 \tag{3.8}$$

in other words, the passage of a gravitational wave modulates the distances between each end mirror and the half-reflective one by a factor h_{11}. So the time for a one way travel along an arm is:

$$\int_0^{t_{and}} dt = \frac{1}{c}\int_0^L \sqrt{1 + h_{11}}dx \approx \frac{1}{c}\int_0^L (1 + \frac{1}{2}h_{11})dx \tag{3.9}$$

the computation for the return is the same, so the total round trip time of the laser beam in the x arm is:

$$\tau_{tot\,x} = \frac{2L}{c} + \frac{1}{2c}\int_0^L h_{11}dx - \frac{1}{2c}\int_L^0 h_{11}dx \tag{3.10}$$

and the analogous expression for the y arm:

$$\tau_{tot\,y} = \frac{2L}{c} + \frac{1}{2c}\int_0^L h_{22}dy - \frac{1}{2c}\int_L^0 h_{22}dy \tag{3.11}$$

Assuming to have a monochromatic plane gravitational wave that propagates along the z direction, with "+" polarization (namely with $h_{11} = -h_{22}$), if $\nu\tau_{tot} \ll 1$ one can consider h as a constant during its passage into the detector, the perturbations in the two arms will have a simple form, and their relative time delay will be:

$$\Delta\tau(t) = h(t)\frac{2L}{c} \tag{3.12}$$

corresponding to a phase shift:

$$\Delta\phi(t) = h(t)\frac{4\pi L}{\lambda} \tag{3.13}$$

where λ is the laser wavelength.

In the general case these two expressions become:

$$\Delta\tau(t) = h(t)\frac{2L}{c}\exp\left(i\pi\nu\frac{2L}{c}\right)\left(\pi^2\nu\frac{2L}{c}\right)^{-1} sin\left(\pi^2\nu\frac{2L}{c}\right) \tag{3.14}$$

and

$$\Delta\phi(t) = h(t)\frac{4\pi L}{\lambda}\exp\left(i\pi\nu\frac{2L}{c}\right)\left(\pi^2\nu\frac{2L}{c}\right)^{-1} sin\left(\pi^2\nu\frac{2L}{c}\right) \tag{3.15}$$

In the low frequency range the detector sensitivity can be expressed in terms of Euler angles, obtaining the so called antenna pattern:

$$\Delta\phi(t) = h(t)\frac{4\pi L}{\lambda}\left[\frac{1}{2}(1 + \cos^2\beta)\cos 2\alpha\cos 2\gamma - \cos\beta\sin 2\alpha\sin 2\gamma\right] \tag{3.16}$$

the detector response is maximum when the wave propagates towards the z direction, when it propagates along x or y direction the response decreases by a factor 2, and it totally cancels for a wave that propagates in the x,y plane with a $\frac{\pi}{4}$ angle with respect to the x or y axes.

3.3 The free falling masses and the attenuation of the resonances

The two mirrors are suspended with a pendulum, so as to be kept in a free fall state: if a gravitational wave passes, the theoretical (considering negligible the dissipations) equation for each mass is

$$m\ddot{x} + \frac{mg}{l}(x - x_0) = \frac{m\ddot{h}L}{2} \tag{3.17}$$

where l is the length of the pendulum suspension, x the mass position, $x_0$the suspension position, L the arm length and $\frac{m\ddot{h}L}{2}$ is the gravitational wave contribution.

For gravitational wave frequency much greater of the pendulum frequency $\omega \gg \omega_0 = 2\pi\sqrt{\frac{g}{l}}$, the mass acts as if it was in a free fall state.

In this regime the only forces they interact with are the gravitational forces, and the dissipations are minimized.

3.3.1 The Virgo suspensions

The Virgo mirrors are suspended in ultra-high vacuum by a cascade of pendula, the so-called super-attenuators, which provide an excellent seismic isolation in the range above the resonance frequencies of the mechanical system (around 1 Hz).

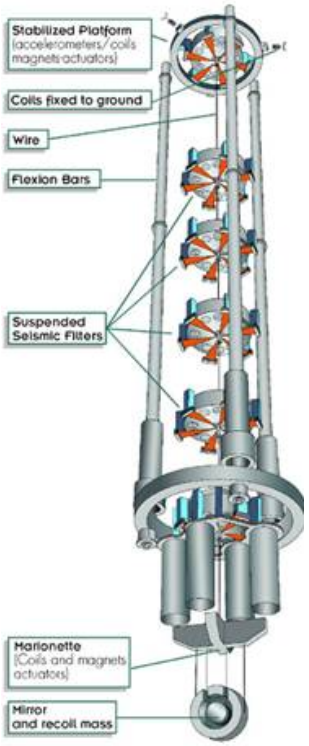

Figure 3.1:
A scheme of the Virgo super-attenuator, taken from http://www.ludotecascientifica.it/virgo.htm

Indeed, the transfer function from the suspension point to the mass can be approximated by:

$$\frac{x(\omega)}{x_0(\omega)} = \prod_{i=1}^{N} \frac{\omega_i^2}{\omega_i^2 - \omega^2} \tag{3.18}$$

and, for frequencies enough above the resonant one,

$$\frac{x(\omega)}{x_0(\omega)} \approx \frac{\prod_{i=1}^{N} \omega_i^2}{\omega^{2N}} \tag{3.19}$$

3.4 The Virgo laser beam path

Virgo uses a laser beam of $20\,W$ power, and 1064 nm of wavelength, generated by a master/slave laser system, with slave high power laser $Nd:YVO_4$, locked to the master laser $Nd:Yag$ (1W) [30].

Its path can be summarized (and simplified) as follows: the beam is split in two orthogonal beams that circulate in the interferometer arms. In order to increase the laser path and consequently improve the detector sensitivity, inside each arm the beam is captured inside a Fabry Perot cavity. The phase of the beam inside the cavity is a function of the cavity length, so if one has a variation of the arm length δL, the corresponding phase shift is [18]:

$$\Delta\phi = 8F\frac{\delta L}{\lambda} \tag{3.20}$$

where F is the so called cavity finesse, which measures the sharpness of the cavity resonance, and it is defined as $F \equiv \frac{\pi\sqrt{R}}{1-R}$. Under the condition $\nu\frac{2L}{c} \ll 1$ (long wavelength), the interferometer response to a gravitational wave event will be [18]:

$$\Delta\phi(\nu) = \frac{8FL}{\lambda} \cdot \frac{h}{\sqrt{1+(\frac{4\nu LF}{c})^2}} \tag{3.21}$$

that gives a different frequency dependence and a gain in detector sensitivity by a factor $\frac{2F}{\pi}$ with respect to a simple Michelson interferometer, whose response function in the general case is [19]:

$$\Delta\phi = \frac{2\pi c\tau_{tot}}{\lambda}\, h\, sinc(\nu\tau_{tot})\, e^{i\,\pi\nu\tau_{tot}} \tag{3.22}$$

The corresponding "effective" path length for the gravitational interferometer results:

$$L_{eff} = L\frac{2F}{\pi} \tag{3.23}$$

Virgo has $L = 3\,km$ and $F = 50$, so its effective path length is about $95\,km$.

The two laser beams are recombined into the half-reflecting mirror; the transmitted signal, corresponding to their interference, is captured by the photo-diodes, where it can be finally analyzed.

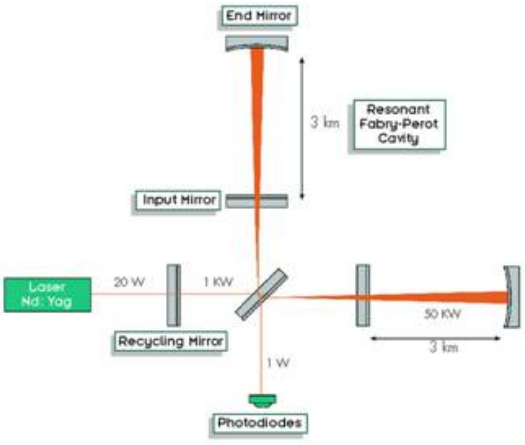

Figure 3.2:
The scheme shows the laser beam path through the interferometer (taken from http://www.ludotecascientifica.it/virgo.htm)

In order to amplify the laser power and reduce the fluctuations due to the shot noise (see paragraph 3.5), the laser first passes through the so called *power recycling*. When the interferometer is in the dark fringe, the light is canalized to the input port, and through the recycling mirror it is reflected with the same phase of the input laser, and the result is an amplification of the laser power into the cavity.

3.5 Noise sources

The interferometer sensitivity to a gravitational wave signal is limited by several sources of noise. These are for simplicity divided into two different categories [18]:

- Mirrors positions fluctuations, due to the ground vibrations (residual seismic noise, and local gravity fluctuations), to the internal noise of mirrors and suspensions (thermal noise, and non-linear effects), and to the noise reintroduction by the active controls of the suspensions.
- Optical readout noise, related with the interferometric readout of the mirror positions, that makes the photo-diode output fluctuate even in absence of signal. It is due to the laser shot noise, as well as to fluctuations of the radiation pressure, of the laser frequency and power.

The noise spectrum $h_n(t)$ is defined as follows:

$$S_n(\nu) = \lim_{T\to\infty} \mid \frac{1}{\sqrt{T}} \int_{-\frac{T}{2}}^{\frac{T}{2}} h_n(t)\, e^{i2\pi\nu t} dt \mid^2 \tag{3.24}$$

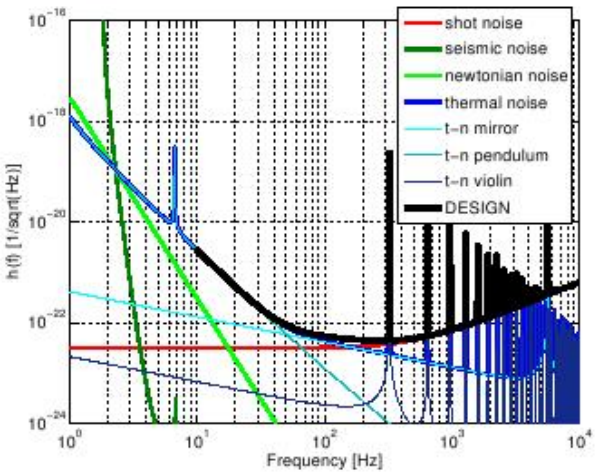

Figure 3.3:
The Virgo design sensitivity curve

The contributions of each noise source as a function of the frequency can be summarized as follow:

- seismic noise below 2 Hz
- thermal noise of the pendulum mode dominating from 10 to 30 Hz
- thermal noise of the mirror modes dominating from 50 to 500 Hz
- thermal noise of the violin modes at peaks above 300 Hz
- shot noise dominating above 500 Hz

Part II

Our gravitational waves source and its method of analysis

Chapter 4

The compact binary systems

4.1 How a binary system evolves through the stars evolution steps.

The history of a binary system is strongly influenced by the initial relative distance between its components.

If the distance is very large ($10^{5\div6} R_\odot$) the interaction with the near "field stars" in the cluster gives many chances to set free the link between the two companions at an early stage of their life.

If the orbit is sufficiently tight to make possible the existence of the system, but still relatively large, each star will evolve separately during the nuclear fusion phases. The only effect will be the orbit circularization and the synchronization between revolution and rotation periods (which causes the orbit to shrink). Circularization and synchronization mechanisms are different [8]: in very eccentric systems the stellar wind can contribute too, moreover the most efficient dissipation mechanism is due to the tidal interactions. Synchronization and circularization typical timescales are much shorter with respect to the stellar evolution typical timescales, so they can be considered instantaneous phenomena. The circularization takes place when the radius of one star is comparable with the orbit separation of the system: $R_1 \geq 0,2\, a_p$, where a_p is the periastron distance. This condition is fulfilled when one of the stars is in the red giant phase of its evolution, or when the system is very tight.

If the relative separation is below 10^4 solar radii there will be interactions and mass exchanges between the two stars.

Under the approximation of newtonian mechanics and circular orbits, the potential in the proximity of the system is [15]:

$$V(x,y,z) = G\frac{m_1}{r_1} + G\frac{m_2}{r_2} + \frac{\omega^2}{2}\left[\left(x - \frac{m_2}{m_1+m_2}a\right)^2 + y^2\right] \tag{4.1}$$

using a reference frame co-rotating with the stars, where the origin is in the heavier one,

and the other one lies on the x axes. Here $\omega = \sqrt{\frac{m_1+m_2}{a^3}}$ is the revolution angular speed.

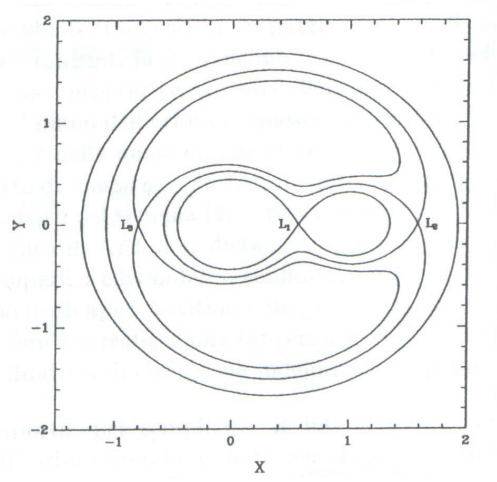

Figure 4.1:
The equipotential surfaces on the orbit plane

The two inner surfaces in fig. 4.1 are called "Roche's lobes", marking the barrier of the potential of the individual field of each star. L_2 and L_3 are the windows used by the system to discard material. When the heavier star expands its radius beyond its Roche's lobe, material begin to flow to the lighter one through L_1. If both the stars expand their radii filling the Roche's lobes, the system experiences the so called "common envelop" phase. During this period the stars move through a high density material, which cause a loss of energy and a consequent shrinking of the orbit.

If both stars have a low mass, after a first common envelop period, the originally heavier companion becomes a dwarf star, now lighter than the other one. A new common envelop phase will occur, with inverted roles, and finally we will have a very tight dwarf system (separation of some solar radii) [15].

The future of massive systems depend on initial separation: if the two stars were not tight enough, when the first reaches the supernova explosion, the system is destroyed. If the two companions were sufficiently close, the explosion enlarges the relative distance, and mass transfer occurs after the explosion, so that the final state will be a tight system of compact objects: neutron stars or black holes.

Hurley, Tout e Pols [8] have provided an example of a double neutron star system birth. They supposed that the orbit is already circularized, and that the kick velocity induced on the companion by the "first" star supernova explosion is negligible. Two stars with initial masses of 13.1 and 9.8 $M_\odot$ orbiting at the initial distance of 138 $R_\odot$ experience the first dynamical mass exchange when the heavier one is a giant star. After a common envelop phase the remnants are an helium star with 3.7 $M_\odot$ and a companion in its main sequence phase which is accreted up to 18.7 $M_\odot$. According to its stellar evolution, the helium star experiences a supernova explosion, and a 1.34 $M_\odot$ neutron star is created. As a consequence of the explosion, the orbit separation slightly increases. When the companion fills its Roche lobe the system experiences a second common envelop phase,

which leaves the "second" star with a reduced mass ($4.6\,M_{\odot}$), the neutron star unchanged and the orbit separation very tight ($1.6\,R_{\odot}$). After the supernova explosion of the second star the result is a double neutron star system with 0.5 days orbital period.

DOUBLE COMPACT OBJECT FORMATION CHANNELS - STANDARD MODEL

Formation Channel	Relative Efficiency [a]	Evolutionary History [b]
NSNS:01	20.3 %	NC:a→b, SN:a, HCE:b→a, HCE:b→a, SN:b
NSNS:02	10.8 %	NC:a→b, SCE:b→a, NC:a→b, SN:a, HCE:b→a, SN:b
NSNS:03	5.5 %	SCE:a→b, SN:a, HCE:b→a, HCE:b→a, SN:b
NSNS:04	4.0 %	NC:a→b, SCE:b→a, SCE:b→a, SN:b, HCE:a→b, SN:a
NSNS:05	3.2 %	DCE:a→b, SCE:a→b, SN:a, HCE:b→a, SN:b
NSNS:06	2.5 %	SCE:a→b, SCE:b→a, NC:a→b, SN:a, HCE:b→a, SN:b
NSNS:07	2.2 %	NC:a→b, NC:a→b, SN:a, HCE:b→a, HCE:b→a, SN:b
NSNS:08	2.0 %	NC:a→b, DCE:b→a, SN:a, HCE:b→a, SN:b
NSNS:09	2.0 %	DCE:a→b, DCE:a→b, SN:a, SN:b
NSNS:10	1.6 %	NC:a→b, SCE:b→a, SN:b, HCE:a→b, SN:a
NSNS:11	1.5 %	NC:a→b, SCE:b→a, DCE:b→a, SN:a, SN:b
NSNS:12	1.5 %	NC:a→b, SCE:b→a, DCE:a→b, SN:a, SN:b
NSNS:13	1.0 %	DCE:a→b, SN:a, HCE:b→a, SN:b
NSNS:14	3.0 %	all other
BHNS:01	4.5 %	NC:a→b, SN:a, HCE:b→a, SN:b
BHNS:02	1.6 %	NC:a→b, SCE:b→a, SN:a, SN:b
BHNS:03	1.3 %	SCE:a→b, SN:a, HCE:b→a, NC:b→a, SN:b
BHNS:04	2.0 %	all other
BHBH:01	17.7 %	NC:a→b, SN:a, HCE:b→a, SN:b
BHBH:02	10.5 %	NC:a→b, SCE:b→a, SN:a, SN:b
BHBH:03	1.4 %	all other

[a]Normalized to the total DCO population.

Figure 4.2:
In the table [4] the principle formation channels of compact systems are listed.
a is the primary star, b the secondary one and the legend is:
NC: non conservative mass transfer
SCE: single common envelop phase
DCE: double common envelop phase
HCE: common envelop with hypercritic mass transfer
SN: supernova explosion

Compact binary systems progressively lose their orbital energy by gravitational waves emission. This mechanism acts as a positive feedback, since the emission increases with the decrease of the relative distance, pushing further the two stars towards merger and collapse into a black hole.

These sources are promising candidates for the gravitational waves ground detectors, also because the waveform is very well modeled (see paragraph 4.4.2)

4.2 Evolution of the "stars community" inside a stellar cluster

Newborn stellar clusters have an irregular shape, due to their "cloudy origins". Little by little the interactions between stars makes the cluster reach its stable configuration, moulding it into a spherical shape (globular cluster), whose density drops moving away from the core ($\rho_{nucl} \sim 10^{-1} \div 10^{6} M_{\odot}/Pc^{3}$). The cluster is a N-body system, where N is

in the range $10^4 \div 10^7$ depending on its dimension. The relaxation time, namely the time needed by the gas of stars to reach the thermal equilibrium, is determined by gravitational interactions between stars. Typical values of relaxation time are 10^9 years, shorter with respect to the ages of cataloged globular clusters, so we can suppose that they have already reached their stable thermal configuration [8]. This is not yet true for the galaxies, which are composed by a much larger number of stars, and they have not completely reached their stable thermal configuration, even if we can distinguish the elder ones due to their elliptical shape.

As soon as the protostars begin to form, the proto-cluster starts to collapse searching for a stable configuration. Initially positions and velocities are quite uniformly distributed among the stars. As a consequence, the massive stars have a greater kinetic energy. Scatterings between stars become more frequent as the cluster collapses, making possible the energy transfer from heavier to lighter stars. Due to the so called "virialization" heavier stars tend to cluster through the cluster core (mass segregation process). When the cluster becomes "globular", namely after 10^9 years, the stars with masses above 2 solar masses have extinguished their "nuclear fuel" becoming compact objects, so the center of the cluster population is mainly composed by degenerate compact objects.

The survivor binary systems have a binding energy much greater then the average kinetic energy of an object in the cluster, so actually they can be considered as a single body in the global mechanics.

Tidal capture is an alternative formation channel for new binary systems. This mechanism acts when two stars move so close to cause strong tidal interaction between them, which lead to excite non-radial oscillations in the stars. If the energy absorbed in the oscillations is large enough to leave the two objects with a negative total energy, a new binary system is born. Nevertheless this phenomenon is quite rare, since in most of the cases the tidal effects are so strong to make the two stars coalesce immediately.

Transformations of existing systems are more ordinary events in the "every-day-life" of a cluster. The resulting objects after these transformation are often tighter systems, and with heavier components with respect to the initial double stars. When a binary system interacts with a single or double field star three different scenarios are possible: the complete disruption of the system, an energy exchange between one component and the single star, or the substitution of one component with the single star. After the scattering the interaction energy is shared among the objects, so the lighter star acquires the biggest velocity, and consequently the higher escape probability.

This kind of interaction is very complex, and astrophysicists have to use numerical simulations. However, as a general rule, if the binding energy of the system is strong (i.e. big with respect to the average kinetic energy of the stars in the cluster) after the scattering the orbit will be shrunk, since part of the gravitational energy is used to thermalize the velocity of field star to the system velocity. If instead, the system is wide, the field star will give its energy to the system, making its bond even weaker. This is the

so called "Heggie's law" : Strong systems become stronger, weak ones become weaker.

The average kinetic energy of the field stars in a cluster depends on its average temperature:

$$\left\langle mv^2 \right\rangle = 3k_B T \tag{4.2}$$

where k_B is the Boltzmann constant. Numerical studies [16] concerning tight systems interactions show that each interaction makes the bond energy 20% stronger on average. Since the number of the scatterings is proportional to the orbit major semi-axes (which is in inverse proportion to the bond energy of the system), the rate of consolidation of the bond results energy independent: $\Delta E \sim -0,6\frac{k_B T}{t_{rel}}$ where t_{rel} is the thermal relaxation time of the cluster. From these simulations, astrophysicists have noticed that with the exchange interactions the mass distribution of binary components tends to increase, so relativistic double stars seems to be favored by the cluster mechanic and thermodynamic mechanisms.

The black hole cases is different, since their progenitors evolve too quickly with respect to the cluster relaxation time. Due to the mass segregation they are attracted in the core, and they create a little sub-cluster there. The binary system with a black hole and a lighter star tend to be disrupted by the exchange with the field heavier objects (black holes).

4.3 Rate of coalescing binaries events

The coalescing binaries rate depends on stellar masses and evolution models. J. A. de Freitas Pacheco, T. Regimbau, S. Vincent and A. Spallicci [32] have computed an estimate of galactic merging rate based both on population synthesis of the pulsar population and on simulations on the evolution of massive binaries, in which they included the star formation history of our Galaxy, derived directly from observations.

Since elliptical galaxies too contribute to the morphological composition of galaxies in the local universe, they estimated the expected coalescence rate in these kind of galaxies, by adopting a star formation model able to reproduce their observed photometric properties. The local average coalescence rate has been thus estimated and weighted according to the total light fraction contribution of each morphological type of galaxies.

In order to compute the galactic coalescence rate, they used the formula:

$$\nu_c(t) = f_B \beta_{NS} \lambda \int_{\tau_0}^{t-\tau_*-\tau_0} P(\tau) R(t-\tau_*-\tau)\, d\tau \tag{4.3}$$

where f_B is the fraction of massive stars binary systems formed among all stars, β_{NS} is the fraction of binaries that remain bounded after the second supernova event, λ is the fraction per unit mass of stars in the mass range $9 - 40\, M_\odot$, $P(\tau)$ is the probability per

unit of time for a newly formed NS-NS binary to coalesce in a timescale τ , τ_* is the mean evolutionary timescale for the massive system to evolve into a neutron stars one (of the order of $10^7 - 10^8\, yr$), τ_0 is the assumed minimum coalescence time, and $R(t)$ is the star formation rate evaluated in $M_\odot \cdot yr^{-1}$.

λ has been computed using the Salpter's law for the initial mass distribution $\xi(M) = k\, M^{-\gamma}$with $\gamma \approx 2.35$, which gives $\lambda = \int_{9M_\odot}^{40M_\odot} \xi(M)\, dM = 5.72 \cdot 10^{-3} M_\odot^{-1}$. They performed numerical simulations, from which they derived the values for the others parameters. Their ingredients for creating a reasonable binary system are the following: they computed the mass of the primary according with a probability distribution corresponding to a Salpeter's law, the secondary mass is derived from the observed mass ratio distribution for massive binaries coming from observations. The orbital separation between stars a is fixed by a probability distribution $P(a) \propto \frac{da}{a}$ ranging from the minimum value, twice the value of the Roche lobe of the primary, up to one hundred times it.

Their simulations indicate a minimum coalescence timescale $\tau_0 = 2 \cdot 10^5 yr$ and a considerable number of systems having coalescence timescales higher than the Hubble time. Using the numbers obtained, it results for the present galactic NS-NS coalescence rate

$$\nu_{c\,Gal} = (1.7 \pm 1.0) \cdot 10^{-5}\, yr^{-1} \tag{4.4}$$

whose estimated error is mostly due to uncertainties in the ratio between the number of single pulsars and the number of binary neutron stars derived from simulations.

Rescaling this number, taking into account of the spiral and elliptical galaxies, they obtained the local mean weighted NS-NS coalescence rate:

$$\nu_{c\,Loc} = 3.4 \cdot 10^{-5}\, yr^{-1} \tag{4.5}$$

4.4 Coalescing binaries as gravitational waves sources

4.4.1 A bit of history: the binary pulsar B1913+16

One of the most beautiful validation of the General Relativity among the last 30 years has been given by neutron stars binary systems, that allow to measure the first experimental evidence of the existence of gravitational waves.

In 1974 Hulse and Taylor discovered a pulsar with "strange" peculiarities. A pulsar (pulsating radio source) is a radio-source emitting very short pulses at regular intervals, with a period ranging from a few seconds to milliseconds. Since the pulsation is related with the object rotation, from the shortness of the signal one can argue that given its very small dimension, the object can be nothing but a neutron star.

As a simple check one can estimate the rotation period of a neutron star with solar mass and angular momentum, but radius 10 Km: assuming an uniform compression starting from the current solar dimensions[1] as the radius will experience a reduction by a factor $7 \cdot 10^4$, the momentum of inertia will be reduced by a factor $5 \cdot 10^9$, and a consequent rotation period of 0.5 ms, perfectly compatible with the hypothesis that traces back a pulsar to a neutron star.

The emission mechanism is another consequence of the star collapse, indeed the "common" dipole magnetic field of the star after the collapse rapidly increases due to the magnetic flux conservation, and the star acquires a large polar magnetic field. The magnetic polar axes is unlikely to coincide with the rotational one, and the neutrons in the external layers of the star are unstable, so they decay forming high energy electrons. These electrons travel across the magnetic field, emitting synchrotron radiation strongly collimated in the magnetic axes direction. As a consequence, due to the spinning of the star, the radiation is emitted in a cone-shaped way. This emission is obviously not free in term of kinetic energy for the star, that slowly decreases its spin.

Hulse and Taylor have monitored a 59 ms period pulsar, and they observed a frequency variation of $-2.47583(2) \cdot 10^{-15} s^{-2}$ due to the energy loss by synchrotron radiation. But they discovered another periodic variation in the pulsation with period 27906.9807804(6) s, and relative amplitude of about 10^{-3}, that they interpreted as a Doppler effect due to the presence of a binary companion of the star. Using the third Kepler's law, from the orbital period they extrapolated a value for the expression $\frac{a^3(m_1+m_2)^2}{m_2^3}$ where a is the orbital semi-mayor axes, and assuming masses of the order of the solar mass, this gives an $a \simeq 2 \cdot 10^6$ km, that is a little more than the solar diameter, and an ellipticity $e \simeq 0.62$.Such a tight system could be a double neutron star system only [7].

The system was so tight that requires the use of General Relativity, and this permitted to refine the scientists knowledge about the two stars: first of all the frequency variation was not only due to the Doppler effect, there were also a significant gravitational redshift in the companion star field (about $3 \cdot 10^{-5}$ between apoastron and periastron), and a delay of the light due to the presence of the masses. Moreover, from an accurate study of the orbital motion they observed a periastron shift (another effect present in the Einstein theory) of $4.226621(11)^\circ/year$. From the comparison between theory and observations Hulse and Taylor could extrapolate the masses of the stars: $m_1 = 1,4410(5)\, M_\odot$ and $m_2 = 1,3784(5)\, M_\odot$.

Observations extended in time revealed an additional feature: the orbital period was decreasing with time:

$$\dot{T} = -2,422(6) \cdot 10^{-12} \tag{4.6}$$

[1]For clarity's sake, we report the most important solar parameters: $M_\odot = 2 \cdot 10^{33} g$, $R_\odot = 7 \cdot 10^5 km$, $L_\odot = 3.84510^{33} erg\, s^{-1}$, $T_{rot} \sim 27\, days$

this implied a shrinkage of the orbit, and an energy loss rate for the system

$$\dot{E} \simeq -5,6 \cdot 10^{31} erg \cdot s^{-1} \tag{4.7}$$

where the total energy was $-9,67 \cdot 10^{47} erg$.

The only mechanism that could explain the phenomenon was the gravitational waves emission.The theoretical computation of the emission, according to the Einstein's General Relativity was:

$$\dot{E} = -\frac{32}{5} \frac{G^4 m_1^2 m_2^7}{c^5 a^5 (m_1+m_2)^4} \frac{1+\frac{73}{24}e^2+\frac{37}{96}e^4}{(1-e^2)^{\frac{7}{2}}} \tag{4.8}$$

in the m_1 reference frame.

A comparison between theory and observation has been done during 20 years of monitoring, with as result the ratio between theoretical and measured energy loss: $1,0032 \pm 0,0035$, a spectacular agreement which earned to the two physicists the Physics Nobel Award in 1993 [23].

4.4.2 The chirp: the gravitational wave signal emitted by a compact system

The gravitational quadrupole of a binary system is given by :

$$Q_{ij} = 2\eta \left(v_i v_j - \frac{M}{a} \hat{n}_i \hat{n}_j \right) \tag{4.9}$$

where $\eta \equiv \frac{m_1 m_2}{(m_1+m_2)^2}$, $\hat{n}_i$ and $\hat{n_j}$ are the two polarization direction vectors, M the total mass and a the orbital distance between the two stars.

In order to fix the order of magnitude of the signal emitted we will take a very simplified model: twin stars with masses m and circular orbit. The quadrupole becomes $Q \sim M\,a^2$and consequently $\dddot{Q} \sim \frac{Ma^2}{T^3} \sim Ma^2\omega^3$. Since from the third Kepler's law we have that $\omega \propto \sqrt{\frac{m}{a^3}}$, we find that:

$$\dddot{Q} \sim \left(\frac{M}{a} \right)^{\frac{5}{2}} \tag{4.10}$$

This formula suggests tight systems as best sources, where the relative distance reaches the order of magnitude of their Schwarzschild's radius.

The temporal evolution of the gravitational waves emission for this kind of source can be divided into three phases:

1. the inspiral, during which the two stars progressively become closer until their first contact (tidal contact, because of their high compactness). Both the signal amplitude and the frequency increase with time, until the "last stable orbit" is reached, the last position of instantaneous equilibrium for the orbit. In this work we will be only concerned by this phase of emission.

2. The merger phase, during which the "fusion" between the two objects occurs. The equation for the gravitational waves emission strongly depends on the models for the equation of state of the neutron stars, or on numerical simulations about the geometry generated by two black holes in collision.

3. The ring-down, the residual emission after the birth of the new black hole. The signal approximately consists in a damped sinusoid, related with the Quasi Normal Modes of the newborn black hole.

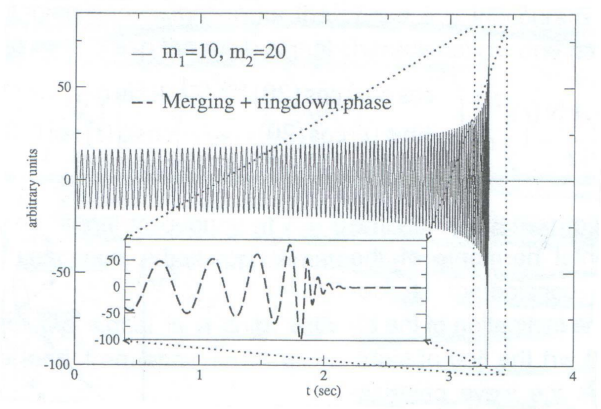

Figure 4.3: Example of a chirp

For a circular orbit (when the signal enters in the detectable frequency range the orbit circularization is mostly completed), the inspiral signal assumes the form:

$$\begin{aligned} h_+ &= A\,[\nu(t)]^{\frac{2}{3}}\cos\phi(t) \\ h_x &= A\,[\nu(t)]^{\frac{2}{3}}\sin\phi(t) \end{aligned} \tag{4.11}$$

where $A \sim \frac{(GM_c)^{\frac{5}{3}}}{r}$ is the wave amplitude, a function of the source distance r and of the chirp mass, defined as $M_c \equiv \frac{(m_1 m_2)^{\frac{3}{5}}}{(m_1+m_2)^{\frac{1}{5}}}$.

$\phi(t)$ is the phase of the signal, in the case of Newtonian approximation given by:

$$\phi(t) = \frac{16\pi\nu_0\tau(\nu_0)}{11}\left[1-\left(1-\frac{t}{\tau(\nu_0)}\right)^{\frac{5}{8}}\right] \tag{4.12}$$

where ν_0 is the frequency at the instant $t = 0$, $\tau(\nu_0)$ is the chirp time, the remaining time before the coalescence.

The gravitational waves frequency is twice the orbital one due to the quadrupolar origin of the gravitational radiation, and is given by:

$$\nu(t) =)\nu_0\left(1-\frac{t}{\tau(\nu_0)}\right)^{-\frac{3}{8}} \tag{4.13}$$

It is interesting to compute how long a signal will stay in the detectable frequency

range:

$$\Delta t = \tau(\nu_0)\left[\left(\frac{\nu_{min}}{\nu_0}\right)^{-\frac{8}{3}} - \left(\frac{\nu_{max}}{\nu_0}\right)^{-\frac{8}{3}}\right] \tag{4.14}$$

The expression for the signal given by 4.11 is computed in the source reference frame. To a terrestrial observer it will assume the form:

$$\begin{aligned} h_+ &= A\ [\nu(t)]^{\frac{2}{3}}\left[\cos\phi(t)\cos(2\psi)\tfrac{\cos^2\epsilon+1}{2} + \sin\phi(t)\sin(2\psi)\cos\epsilon\right] \\ h_x &= A\ [\nu(t)]^{\frac{2}{3}}\left[\sin\phi(t)\cos(2\psi)\cos\epsilon - \cos\phi(t)\sin(2\psi)\tfrac{\cos^2\epsilon+1}{2}\right] \end{aligned} \tag{4.15}$$

where ϵ describes the orbit inclination with respect to the line of sight, ψ the ellipse polarization angle.

It is also possible to refine the Newtonian waveform adding the so called "Post-Newtonian" corrections. The Post-Newtonian formalism is a Taylor expansion starting from the weak field for the gravitational potential, and from the "slow source" ($\frac{v}{c}$ power series) where the zero-th order is the Newtonian approximation, and the corrections are due to the General Relativity.

The signal using the correction of the second Post-Newtonian order (2PN) has the same general form as in the Newtonian case, but the phase is given by:

$$\begin{aligned} \phi(\nu) = \tfrac{16\pi\nu_r\tau_0}{5}\Bigg[&\left(1-\left(\tfrac{\nu}{\nu_r}\right)^{-\frac{5}{3}}\right) + \tfrac{5\tau_1}{4\tau_0}\left(1-\left(\tfrac{\nu}{\nu_r}\right)^{-1}\right) + \\ &-\tfrac{25\tau_{1,5}}{16\tau_0}\left(1-\left(\tfrac{\nu}{\nu_r}\right)^{-\frac{2}{3}}\right) + \tfrac{5\tau_2}{2\tau_0}\left(1-\left(\tfrac{\nu}{\nu_r}\right)^{-\frac{1}{3}}\right)\Bigg] \end{aligned} \tag{4.16}$$

where ν_r is an arbitrary reference frequency, τ_i are the corrections to the Newtonian chirp time, defined as:

$$\begin{aligned} \tau_0 &\equiv \tfrac{5}{256\pi}\nu_r^{-1}(\pi M\nu_r)^{-\frac{5}{3}}\eta^{-1} \\ \tau_1 &\equiv \tfrac{5}{192\pi}\nu_r^{-1}(\pi M\nu_r)^{-1}\left(\tfrac{753}{336}+\tfrac{11}{4}\eta\right)\eta^{-1} \\ \tau_{1,5} &\equiv \tfrac{1}{8}\nu_r^{-1}(\pi M\nu_r)^{-\frac{2}{3}}\eta^{-1} \\ \tau_2 &\equiv \tfrac{5}{128\pi}\nu_r^{-1}(\pi M\nu_r)^{-\frac{1}{3}}\left(\tfrac{3058673}{1016064}+\tfrac{5429}{1008}\eta+\tfrac{617}{144}\eta^2\right)\eta^{-1} \end{aligned} \tag{4.17}$$

and η is the ratio between reduced and total mass of the system.

The wave frequency is the solution of the differential equation:

$$\frac{d\nu}{dt} = \frac{3\nu_r}{8\tau_0}\left(\frac{\nu}{\nu_r}\right)^{\frac{11}{3}}\left[1 - \frac{3\tau_1}{4\tau_0}\left(\frac{\nu}{\nu_r}\right)^{\frac{2}{3}} + \frac{5\tau_{1,5}}{8\tau_0}\left(\frac{\nu}{\nu_r}\right)^{\frac{11}{3}} - \frac{1}{2}\left(\frac{\tau_2}{\tau_0} - \frac{9}{8}\left(\frac{\tau_1}{\tau_0}\right)^2\right)\left(\frac{\nu}{\nu_r}\right)^{\frac{4}{3}}\right] \tag{4.18}$$

4.4.3 Expected detection rate

Using their calculation for the coalescence rate, J. A. de Freitas Pacheco, T. Regimbau, S. Vincent and A. Spallicci [32] computed the expected detection rate for Virgo and LIGOs experiments. They used their planned sensibility, and obtained one event each 148 years

for Virgo, and one event each 125 years for LIGO.

The future proposed Advanced Virgo configuration may significantly raise the expected detection rate up to 3 events every two years, and for Advanced LIGO, 6 events per year are expected to be seen.

As for the present, the rates can be improved considering a network of three detectors (Virgo, Hanford and Livingston) operating in a coherent mode, since in this case the expected rate corresponds to one event each 26 years.

Chapter 5

Analysis with a single detector

5.1 The matched filtering technique

Since the inspiral signal coming from coalescing binaries is quite well known (see paragraph 4.4.2), the technique that suites at best with this kind of signal is the so called matched filtering method. More in details, because of the uncertainty of the effective detection of a gravitational wave, one has to work with the detection probability and try to maximize it. For this kind of signals the more appropriate statistic to be maximized is the likelihood, defined as the ratio between the probability that the data contain effectively a signal and the probability that they contain just noise.

According to the matched filtering technique one has to filter the data stream using a theoretical template, varying its parameters until the superposition between data and template reaches its maximum.

Assuming that the noise is an additive function, the output of a detector will be:

$$x(t) = s(t) + n(t) \tag{5.1}$$

where in absence of signal, $s(t) = 0$.

The Wiener correlation between data stream and template is defined as follow [1]:

$$< s, x >= 2\Re \int_0^\infty \frac{\tilde{s}^*(\nu)\tilde{x}(\nu)}{S_h(\nu)} d\nu \tag{5.2}$$

where $\tilde{x(\nu)}$ and $\tilde{s(\nu)}$ are the Fourier transforms of the data stream and of the template, $S_h(\nu)$ is the power spectral density of the detector noise.

Under the assumption of entirely gaussian noise, the likelihood can be expressed in terms of the scalar product induced by the correlation:

$$LR = \frac{\exp(-\frac{1}{2} < x - s,\, x - s >)}{\exp(-\frac{1}{2} < x,\, x >)} \tag{5.3}$$

The expression becomes easier to handle if one uses its natural logarithm:

$$LLR =< s,\, x > -\frac{1}{2} < s,\, s > \tag{5.4}$$

Since the observer does not know when the "candidate" gravitational waves event will occur, one has to comb all the data stream "sweeping" the template over that. The correlation C between data and template becomes in this way a time-dependent function:

$$C(t) \equiv < s_t,\, x(t) >= 2\Re \int_0^\infty \frac{\tilde{s_t}^*(\nu)\tilde{x}(\nu)}{S_h(\nu)} d\nu \tag{5.5}$$

This procedure has to be done for all the different values of the template parameters. More in details, once the template is chosen, one has to set, for all the parameters included in the template, a physically interesting range. The set of intervals and their spacings form the so called parameters grid. The spacings have to be set choosing the best compromise between accuracy of the detection and computational costs.

Using the Newtonian approximation, we have seen that a coalescing binary signal depends on several parameters: the stars masses, their sky position, their distance, the coalescence time (instant at which the two stars begin to merge), the phase of the wave at coalescence time, the wave polarization, the orbit inclination with respect to the line of sight. With a single detector one can determine the masses of the stars, and extrapolate the so called best oriented distance, that is the distance of the source if it were optimally oriented with respect to the interferometer.

For the purpose of explaining the matched filter technique, one can write the coalescing binaries Newtonian signal as follow:

$$s_t = A\, [\nu(t)]^{\frac{2}{3}}\, e^{\frac{16\pi\, i\, \nu\tau(\nu_0)}{11}\left[1-\left(1-\frac{t}{\tau(\nu_0)}\right)^{\frac{5}{8}}\right]} \tag{5.6}$$

where ν_0 is the detection starting frequency and the wave amplitude A contains such stellar information like the source distance and its orbit inclination with respect to the line of sight, that cannot be extrapolated using a single interferometer. The signal finally depends on a single parameter (from the parameter estimation point of view), the signal duration τ, from which one can determine the masses of the stars.

From the computational costs point of view the arrival time is the less expensive parameter, since one can notice that two templates that are identical but for the arrival time, in the Fourier space differ only by a phase shift [21]:

$$C(t+\Delta t) \equiv < s_{t+\Delta t},\, x(t) >= 2\Re \int_0^\infty \frac{\tilde{s}^*_{t+\Delta t}(\nu)\tilde{x}(\nu)}{S_h(\nu)} d\nu = 2\Re \int_0^\infty \left[\frac{\tilde{s_t}^*(\nu)\tilde{x}(\nu)}{S_h(\nu)}\right] e^{2\pi\, i\, \nu\, \Delta t} d\nu \tag{5.7}$$

the last member of the equation is indeed the inverse Fourier transform of the correlation between signal and the first template computed at the point $t + \Delta t$.

Thus, supposing to have N samples (ranging from t to $t + N\,\Delta t$) and that the number of operations needed to compute the correlation $C(t)$ are $n(N)$, if one has to repeat the

operation for all the possible arrival times of the samples the total operations will be $n(N^2)$. If instead one evaluates first the integrand $\frac{\tilde{s}_t{}^*(\nu)\tilde{x(\nu)}}{S_h(\nu)}$ for all the frequency values determined by the samples, and then computes the inverse Fourier transform, uses only $n(N\,ln\,N)$ operations [21].

If the data actually contain a signal compatible with one of the templates, its corresponding correlation will present a bell-shape, with the peak at the time at which signal and template have best overlap, namely the detector arrival time.

"In the real life", it is unlikely that a template perfectly overlap a signal, both due to the discrete samples, and to the detector systematic noise. Supposing to have the signal that can be perfectly described with the set of parameters θ

$$s_\theta(t) = A_\theta \widehat{s}_\theta(t) \tag{5.8}$$

and that the template with best correlation have a set of parameters θ_1 and an arrival time $t + \Delta t$, so the correlator will be:

$$C_{\theta\,\theta_1}(t + \Delta t) =< \widehat{s}_\theta(t),\, \widehat{s}_{\theta_1}(t + \Delta t) > \tag{5.9}$$

For this kind of signal a difference in the parameters can be partially balanced by a slight shift of the arrival times: if one maximize the correlation over this parameter can thus obtain a larger overlap, and define in this way the so called ambiguity function:

$$C_{\theta\,\theta_1} = \underset{\Delta t}{max} < \widehat{s}_\theta(t),\, \widehat{s}_{\theta_1}(t + \Delta t) > \tag{5.10}$$

this is the expression for one quadrature, the general formula for the sum of the quadrature is:

$$C_{\theta\,\theta_1} = \underset{\Delta t}{max} \sqrt{< \widehat{s}_{\theta\,0}(t),\, \widehat{s}_{\theta_1\,0}(t + \Delta t) >^2 + < \widehat{s}_{\theta\,\pi/2}(t),\, \widehat{s}_{\theta_1\,\pi/2}(t + \Delta t) >^2} \tag{5.11}$$

From the ambiguity function one can compute the distance between the templates, since it represents how much maximal SNR amplitude a certain template can recover from a signal that is not perfectly matched.

A very simple example can be done using the newtonian signal. It has only one parameter τ, that is related with the chirp mass of the system M_c by the relation [21]:

$$\tau = 3 \left(\frac{M_c}{M_\odot}\right)^{-5/3} \left(\frac{\nu_0}{100Hz}\right)^{-8/3} s \tag{5.12}$$

choosing 40 Hz as detection starting frequency, if one set the spacing between samples at 20 ms so that the corresponding loss in SNR will be about 15%. Depending on the mass range that one want to search for, the number of template will change. If one sets the

minimum chirp mass as 0.25 $M_\odot$, the resulting signal duration will be around 350 ms, therefore one will need about $1.7 \cdot 10^4$ different time samples.

Using the post-Newtonian corrections but neglecting the spin effects, the parameter space becomes two-dimensional, one has the template depending on τ_0 and τ_1, that allows to determine the two star masses, m_1 and m_2 [21].

5.2 The two Virgo analysis pipelines

As we have seen in the previous example, the computational costs of an inspiral search are very high. In the Virgo experiment two different methods of analysis has been developed: one based on flat parallel search, the Digital Signal Analyzer, known as Merlino, and the other based on a multi-band template search, MBTA. In the next two paragraphs we will try to summarize how those pipelines work.

5.2.1 MBTA [22]

The basic idea of the multi-band-template method is that splitting the analysis in several frequency bands the computational costs can be reduced with respect to the "classical" matched filtering search. We have seen that the matched filter is most efficient if applied in the frequency domain, and the MBTA pipeline uses this advantage in this sense, splitting the correlation integral in different bands:

$$C(t) = 2\Re \int_0^\infty \frac{\tilde{s_t}^*(\nu)\tilde{x}(\nu)}{S_h(\nu)} d\nu = 2\Re \int_{\nu_0}^{\nu_{Max}} \frac{\tilde{s_t}^*(\nu)\tilde{x}(\nu)}{S_h(\nu)} d\nu = \tag{5.13}$$

$$2\Re \left[\int_{\nu_0}^{\nu 1} \frac{\tilde{s_t}^*(\nu)\tilde{x}(\nu)}{S_h(\nu)} d\nu + \int_{\nu_1}^{\nu_{Max}} \frac{\tilde{s_t}^*(\nu)\tilde{x}(\nu)}{S_h(\nu)} d\nu \right]$$

where ν_0 is the minimum frequency detectable by the interferometer, ν_{Max} the signal maximum frequency, and ν_1 the cutting frequency between the two bands. The computational costs are reduced for two reasons: the first is the reduction of the number of templates, that is due to the shortening of the signal, especially in the high frequency band. The other reason is related with the decrease of the size of the FFTs, due both to the shortening of the signal, both to the fact that using a restricted bandwidth one can reduce the sampling rate.

This procedure is also perfectly suited to a hierarchical search, since the matched filter is applied at each band separately, and one can analyze first the narrower ones, reducing the number of candidate templates, and then work with the remaining larger bands.

At the end of the search one has to coherently recombine the whole signal, since the correlation has to be exactly as in the case of simple matched filtering. The coherent recombination has to be done before taking the quadratic sum of the two template

quadratures, indeed the two quadratures of an inspiral signal enter the frequency bands at different times and with different initial phases. Thus in recombining each correlator quadrature, one has to make a time translation and a phase rotation:

$$C_0(t) = C_{0\,\nu_0\to\nu_1}(t) + \cos\Delta\phi \cdot C_{0\,\nu 1\to\nu_{Max}}(t+\Delta t) + \sin\Delta\phi \cdot C_{\frac{\pi}{2}\,\nu 1\to\nu_{Max}}(t+\Delta t) \quad (5.14)$$

$$C_{\frac{\pi}{2}}(t) = C_{\frac{\pi}{2}\,\nu_0\to\nu_1}(t) + \cos\Delta\phi \cdot C_{\frac{\pi}{2}\,\nu 1\to\nu_{Max}}(t+\Delta t) + \sin\Delta\phi \cdot C_{0\,\nu 1\to\nu_{Max}}(t+\Delta t) \quad (5.15)$$

where $\Delta\phi$ and Δt depend on each template parameters.

In order to make a brief summary, one can say that the MBTA Virgo pipeline works essentially as follows: it has several template banks used to perform the matched filtering in the restricted frequency bands, and other template banks associated with the whole band, used for the recombination of the signal. The matched filter procedure works in parallel for all the frequency bands, and then starts the combination process, that can be done systematically in case of flat search, or triggered by the results of the reduced search in case of hierarchical search.

5.2.2 Merlino [28]

The basic idea of the Distributed Signal Analyzer (DiSA, better known as Merlino) is a parallelization of the processes, using several CPUs in order to drastically reduce the computational time. The templates generation and the matched filter are performed simultaneously by different CPUs intercommunicating that use an asynchronous scheme based on MPI protocol. The results of each matched filter, namely the correlators, are then sent to a single process that reconstructs and clusterizes the candidate events.

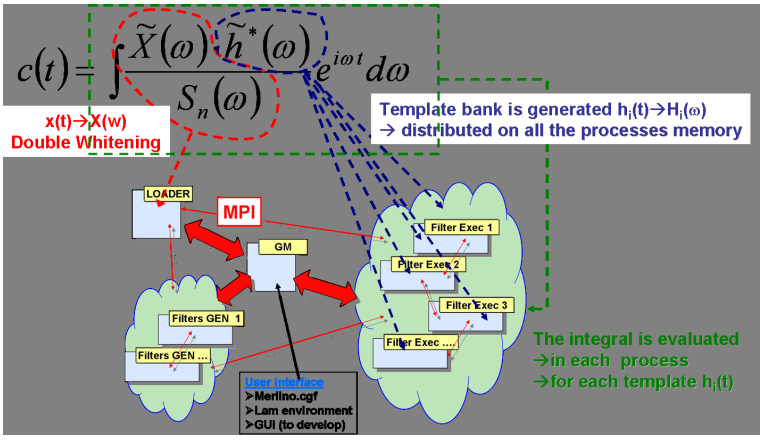

Figure 5.1: Here is a scheme of the pipeline, taken from the poster for [29].

Chapter 6

Network analysis and source position reconstruction

6.1 Introduction: what can be done with a network of interferometers

In order to start a gravitational waves astrophysics it is important to reconstruct as many source parameters as possible, naturally with the best accuracy permitted by the instrumental sensitivity. Gravitational observations of compact objects can help theoretical astrophysics to better understand the behavior of stellar matter in such extreme conditions, and could eventually allow to test the different equations of state in the neutron star models, and for example to fix exactly the upper mass value for a neutron star, which presently depends on the model for the equation of state, or to better understand black holes physics.

From the inspiral phase of a coalescing binary system we should determine the stellar masses, the source distance, its sky position, the orbit inclination with respect to the line of sight, the so called coalescence time (time remaining before the tidal contact between the two objects). The possibility to have a network of interferometers with respect to a single one is quite important from the point of view of the so called *inverse problem*, consisting in the determination of the astrophysically interesting parameters of a binary from the parameters of the detector's response function. In particular, with a single detector we can determine the stellar masses from the signal amplitude, but if we want to extrapolate the stars position we need at least three interferometers in order to make a triangulation.

With a network of three interferometers we can reconstruct the source position modulo a reflection with respect to the detectors plane, to discard the ambiguity a fourth instrument would be necessary. Three interferometers are however a good starting gravitational waves observatory, although, like an electromagnetic one, it cannot distinguish the orbit inclination with respect to the line of sight. An important further improvement is that

the accuracy in the determination of masses and distance increases with the number of the detectors in the network [13].

6.2 Coincidence analysis

The coincidence analysis works essentially with the relative time delays between interferometers. We have said before that with a network of three detectors it is possible to reconstruct the source position modulo a reflection with respect to the interferometers plane.

If we imagine to take a reference frame centered in one of the detectors, we can take:

- as the x axes the direction towards another interferometer (just in order to identify it, we will call it the second one) : $\widehat{x} = \widehat{n_{12}} = \frac{\overrightarrow{L_{12}}}{L_{12}}$,

- as the y axes the vector joining the first and the third detector, orthogonalized respect to the x axes: if $\widehat{n_{13}} = \frac{\overrightarrow{L_{13}}}{L_{13}}$ $\quad \widehat{y} = \frac{\widehat{n_{13}} - (\widehat{n_{12}} \cdot \widehat{n_{13}})\widehat{n_{12}}}{\sqrt{1-(\widehat{n_{12}} \cdot \widehat{n_{13}})^2}}$,

- as the z axis the direction chosen in such way that (x,y,z) is a right-handed coordinate system.

If we call t_{12} , t_{13} the relative time delays between interferometers and $\widehat{k}$ the source direction, we can write the vector k as a linear combination of the (x,y,z) base, obtaining the relation:

$$\widehat{k} = \left(\frac{c\,t_{12}}{L_{12}}\right)\widehat{n_{12}} + \left(\frac{c\,t_{13}}{L_{13}} - \frac{\widehat{n_{12}} \cdot \widehat{n_{13}}\, c\,t1_{12}}{L_{12}}\right)\widehat{y} \pm \sqrt{1 - \left(\frac{c\,t_{12}}{L_{12}}\right)^2 - \left(\frac{c\,t_{13}}{L_{13}} - \frac{\widehat{n_{12}} \cdot \widehat{n_{13}}\, c\,t1_{12}}{L_{12}}\right)^2}\,\widehat{z} \tag{6.1}$$

where the coefficients are the projections of k over the axes, computed imposing that k is a unit vector. From this formula we can extrapolate the two possible source directions, since all the quantities in the right part of the equation are known (c is the light speed, L the relative distances between detectors).

When the direction vector is known, it is easy to reconstruct the astronomic coordinates, declination δ ($\frac{\pi}{2} - \theta$ where θ is the usual polar angle in polar coordinate system) and right ascension ϕ, since we have that:

$$k_x = \cos\delta \cos\phi \tag{6.2}$$

$$k_y = \cos\delta \sin\phi \tag{6.3}$$

$$k_z = \sin\delta \tag{6.4}$$

So, we find:

$$\delta = \arcsin k_z \tag{6.5}$$

$$\phi = \frac{\arctan\left(k_x, k_y\right)}{\cos\delta} \tag{6.6}$$

Looking at that formulas we can see that the accuracy in estimating the sky position is related to the time delays accuracies, so we can suppose that as the network area increases, the uncertainty circle around the stars position becomes smaller. For a more quantitative approach to this problem, see Appendix A.

6.3 Coherent analysis

The basic idea of the coherent analysis is to "construct" an ideal detector equivalent to the network of interferometers, to which each real detector coherently contributes with its sensitivity, position and orientation; and then to proceed with the analysis as in the case of a single detector, such as constructing a statistic which has to be maximized over source parameters in order to find the best template for the arrival signal.

This kind of analysis takes an advantage with respect to the more intuitive coincident one: here all the information coming from each interferometers are used, and, in addition the network of detector too is used at its best, since the relative locations, orientations and relative phases of the signal are combined at best in the network statistic; this is the real meaning of "coherent contribute to the network".

The theory is explained in detail in [1]. We will try to report a brief summary and a tentative (very tentative) popularization of their work.

The optimal network statistic is the logarithm of the likelihood ratio. We have seen in paragraph 5.1, when we have briefly explained the matched filter technique, that the logarithm of the likelihood ratio for a single detector is defined as:

$$LLR = < s, x > -\frac{1}{2} < s, s > \tag{6.7}$$

The same quantity can be defined for the whole network of interferometers, simply taking the sum of each single detector LLR:

$$LLR = \sum_{I=1}^{N} < s^I, x^I >_I - \frac{1}{2} < s^I, s^I >_I \tag{6.8}$$

where N is the number of detectors in the network and, for each interferometer, x^I is the data stream, s^I the template. The cross correlation $<,>$ is the Wiener filter, given by

$$< a, b >_I = 2\Re \int_0^\infty \frac{\widetilde{a}^*(\nu)\widetilde{b}(\nu)}{s_{h_I}(\nu)} d\nu \tag{6.9}$$

where $s_{h_I}(\nu)$ is the so called two sided power spectral density of the $I-th$ detector, defined as:

$$S_{h_I}(\nu) = \lim_{T\to\infty} \mid \frac{1}{\sqrt{T}} \int_{-\frac{T}{2}}^{\frac{T}{2}} h_I(t)\, e^{i2\pi\nu t} dt \mid^2 \tag{6.10}$$

We have seen that for a coalescing binaries signal, using the Newtonian approximation, the signal in the source reference frame assumes the form

$$s_t = A\, [\nu(t)]^{\frac{2}{3}}\, e^{\frac{16\pi\, i\, \nu 0 \tau(f_0)}{11}\left[1-\left(1-\frac{t}{\tau(\nu_0)}\right)^{\frac{5}{8}}\right]} \tag{6.11}$$

if we make explicit each functional dependence from the astrophysical source parameters and from the detector starting frequency ν_s, we obtain:

$$S^I\,(t, t_c) = \frac{G^{\frac{5}{3}} M_c^{\frac{5}{3}}\, (\pi\nu_s)^{\frac{2}{3}}}{r\, c^4} \left[9.69\, (t_c - t)^{-\frac{1}{4}} \left(\frac{M_c}{M_\odot}\right)^{-\frac{5}{12}} \left(\frac{\nu_s}{40\, Hz}\right)^{-\frac{2}{3}}\right] \cdot \tag{6.12}$$

$$\exp -\pi i\, \nu_s \left[12.07\, (t_c - t)^{-\frac{5}{8}} \left(\frac{M_c}{M_\odot}\right)^{-\frac{15}{24}} \left(\frac{\nu_s}{40\, Hz}\right)^{-1}\right]$$

where ν_s is the minimum frequency detectable by the interferometer and M_c is the chirp mass. We note that the signal in this frame contains the so called "intrinsic information", strictly related with the wave generation, which are independent from the source location in the sky, and the observer location.

When (if) an event of this kind will be detected by an interferometer, it will appear in a more complicate form:

$$s^I(t, t_c) = \Re[(EBP_I^* S^I) e^{i\delta_c}] \tag{6.13}$$

where δ_c is the phase of the wave at the instant of the coalescence, and EBP_I is the so called extended beam pattern function of the interferometer, which describes the response

of the detector to the event, and depends on the source position in the sky δ, ϕ, its orbit inclination with respect to the observer's line of sight ϵ, the polarization-ellipse angle ψ, and the interferometer location by the Euler angles to transform coordinates expressed in the standard geocentric frame into coordinates expressed in the i-th detector frame $\alpha_I, \beta_I, \gamma_I$. The extended beam pattern EBP_I can be expressed in terms of the Gel'fand functions of rank 2[1] as follows:

$$EBP^I(\psi, \epsilon, \delta, \phi, \alpha_I, \beta_I, \gamma_I) = g^I T_2^{2\,p}(\psi, \epsilon, 0)\, D_p^I \qquad p = \pm 2 \tag{6.14}$$

where g^I is the detector relative sensitivity with respect to the one chosen as "the fide". The detector sensitivity g^I_{abs} is defined as follow:

$$g^I_{abs} = \left(\frac{4}{3}\,\nu_s^{4/3} \int_{\nu_S}^{\nu_{LSO}} \frac{d\nu}{\nu^{7/3} s_{h_I}(\nu)}\right)^{1/2} \tag{6.15}$$

where $\nu_{LSO}$is the last stable orbit frequency, defined as the orbital frequency of the stable circular orbit closest to the tidal contact between the two stars.

For an interferometer with orthogonal arms

$$D_p^I(\delta, \phi, \alpha_I, \beta_I, \gamma_I) = -i\, T_p^{2\,s}(\delta, \phi, 0)\left[T_s^{2\,2\,*}(\alpha_I, \beta_I, \gamma_I) - T_s^{2\,-2\,*}(\alpha_I, \beta_I, \gamma_I)\right] \tag{6.16}$$

where $s = 0, \pm 1, \pm 2$. D is a complex quantity. The explicit expression for the extended beam pattern is therefore quite "voluminous".

Thus the signal at each detector depends on nine parameters, that can be summarized as follow:

- the intrinsic parameters, strictly related to the wave generation , such as the stellar masses m_1, m_2 through the chirp mass M_c, the source distance r, and the polarization-ellipse angle ψ ($\in [0, 2\pi]$);

- the extrinsic parameters, which influence only the detector output, since they are related to the interferometer position, such as the inclination of the orbit respect to the line of sight ϵ ($\in [0, \pi]$), the source direction δ, ϕ, the coalescence time t_c (final time of the inspiral, when the two stars begin to merge), and the phase of the waveform at the coalescing time δ_c.

As a consequence, the likelihood function too depends on these parameters. Fortunately an analytic maximization is possible over four parameters: source distance r, wave phase at coalescence time δ_c, orbit inclination with respect to the line of sight ϵ,

[1] The Gel'fand functions are defined as:
$T_n^{l\,m}(\alpha, \beta, \gamma) = \exp(-i\,n\,\alpha) \exp(-i\,m\,\gamma)\, \frac{(-1)^{l-m} i^{n-m}}{2^l (l-m)!} \sqrt{\frac{(l-m)!(l+n)!}{(l+m)!(l-n)!}}\, (1-\cos\beta)^{-\frac{n-m}{2}}\, (1+\cos\beta)^{-\frac{n+m}{2}} \cdot \frac{d^{l-n}}{d(\cos\beta)^{l-n}} \left[(1-\cos\beta)^{l-m}\, (1+\cos\beta)^{l+m}\right]$ where the rank l is a natural number, m and n are integers.

and polarization-ellipse angle ψ. After that, the network statistic can be written as a quadratic function of the N detectors correlators [1]:

$$L^2(t) = p_I^J(\delta, \phi, \alpha_I, \beta_I, \gamma_I, \alpha_J, \beta_J, \gamma_J) \cdot \tag{6.17}$$

$$\cdot \left[C_0^I(t - \tau_I(\delta,\phi) C_{0J}(t - \tau_J(\delta,\phi) + C_{\frac{\pi}{2}}^I(t - \tau_I(\delta,\phi) C_{\frac{\pi}{2}J}(t - \tau_J(\delta,\phi) \right]$$

where $C_0^I, C_{\frac{\pi}{2}}^I$ are the two quadratures of the correlators and p_I^J is a matrix with as many rows and columns as the number of detectors in the network, which in turn depends on the interferometer locations, their relative sensitivities, and the source position. We can look at the likelihood as a scalar product between the correlators, where the metric is the p-matrix. The p-matrix can be written using the Gel'fand function of rank 2 and the D_p^I tensors, and the ij-th matrix element assumes the form:

$$p^{IJ} = g^I \frac{\Re D_{+2}^I + \Im D_{+2}^I}{\left\| \Re D_{+2}^I + \Im D_{+2}^I \right\|} \frac{\Re D_{+2}^J + \Im D_{+2}^J}{\left\| \Re D_{+2}^J + \Im D_{+2}^J \right\|} + g^I \frac{\Re D_{+2}^I - \Im D_{+2}^I}{\left\| \Re D_{+2}^I - \Im D_{+2}^I \right\|} \frac{\Re D_{+2}^J - \Im D_{+2}^J}{\left\| \Re D_{+2}^J - \Im D_{+2}^J \right\|} \tag{6.18}$$

it is normalized such that $p^{IJ} p_{IJ} = 2$.

In order to give an idea of the shape of the p-matrix, in the case of very simple network made by the two Hanford interferometers the matrix assumes the form:

$$p = \begin{pmatrix} p_{HH}(\delta,\phi) & 0 \\ 0 & \frac{p_{HH}(\delta,\phi)}{2} \end{pmatrix} \tag{6.19}$$

where the value of p_{HH} only depends on the source position in the sky, and the contribution due to the 2 km interferometer results weighted with its relative sensitivity with respect to the 4 km ones.

If one adds the Livingston detector as third detector, the matrix assumes the form:

$$p = \begin{pmatrix} p_{HH}(\delta,\phi) & 0 & p_{HL}(\delta,\phi) \\ 0 & \frac{p_{HH}(\delta,\phi)}{2} & \frac{p_{HL}(\delta,\phi)}{2} \\ p_{HL}(\delta,\phi) & \frac{p_{HL}(\delta,\phi)}{2} & p_{LL}(\delta,\phi) \end{pmatrix} \tag{6.20}$$

adding an interferometer that is not aligned with them, such as Virgo, the p elements will also depend on the detectors relative orientations.

The LLR finally depends on stellar masses m_1, m_2, the coalescence time t_c, and the source position δ, ϕ.

The maximization over the coalescence time can be done in the frequency domain, where a time translation is only a phase shift of the correlation vector, reducing the computational cost, as in the case of single detector analysis (see paragraph 5.1).

Focusing on the determination of the source position, one should maximize the network statistic over the solid angle of the Celestial sphere. Each position in the sky gives a different set of time delays (actually each couple of specular positions with respect to the three interferometers plane gives a different set), so a chirp search over (δ, ϕ) for a given configuration of network leads to a "window" of time delays. In a network of three detectors there are two independent time delays, which are restricted in a bounded region of a plane, circumscribed by an ellipse. Any point in this region represents a pair of time delay values (τ_2, τ_3) corresponding to a given pair of values for the source direction angles (δ, ϕ). The ellipse equation is given by:

$$\tau_2^2 + \tau_3^2 \left(\frac{L_{13}}{L_{12}}\right)^2 - 2\tau_2\tau_3 \frac{L_{13}}{L_{12}} \cos\alpha_{23} - \left(\frac{L_{13}}{c} \sin\alpha_{23}\right)^2 = 0 \tag{6.21}$$

where L_{12}, L_{13} are the distances between the first and the second (third) detector, and $\alpha_{23}$is the angle subtended by the hubs of interferometers "2nd" and "3rd" at that of the first one.

From this, the number of possible time delays for a network is $2\pi\frac{A}{c^2\Delta^2}$ where A is the area of the triangle formed by the hubs of three detectors, and Δ the time sample of the data. For the network composed by Virgo and the 4 km LIGOs, the number of possible time delays is $\sim 3 \cdot 10^3$. This means that for each event detected by the network we should try $\sim 3 \cdot 10^3$ different templates in order to determine only the sky position, that is computationally very expensive.

6.4 Our work: an hybrid strategy

In order to reduce the computational costs, we have used an hybrid strategy: starting from a coincidence, we have tried to improve the determination of the source position using the coherent analysis. During the work, as better explained later on, our priorities slightly moved towards the removal of the systematic effects in the reconstructed position due to the finite sampling rate of each interferometer, and to the discretization of template grids.

Indeed we have noticed that in the reconstructed positions space (δ, ϕ) not all the positions were allowed: the discrete sampling rate on the detectors is actually translated in a discretization of the arrival times at each detector, and this corresponds to a discretization of the reconstructed source positions. So we have worked on the removal of these effects, and we have reached our aim both with the coincident method, creating an "enhanced coincident method" (obtained using the reference time and a fit of the shape of the individual correlator, as we explain later on) and with the coherent one. As for the latter method, we have obtained the results in a relatively automatic way and in a cheap way from the computational costs point of view.

As a common feature of the different coincident and coherent methods we have tried before finding the best two, in case of real coincidences, the "mirror position" has been discarded. This operation is obviously very simple working with simulated data, since we compare the theoretical position vector with the two reconstructed, and we consider the closer one only. When we will work with a real event, we will have to consider both directions as possible candidates, and use all the possible astrophysical additional information available (an example is the collaboration between gravitational waves and Gamma Ray Bursts, see Appendix B) in order to distinguish between them: the most direct is to search for an electromagnetic or neutrinos counterpart of the explosion.

6.5 First test of the method: maximization over one detector correlator

Our first test was very simple. We have computed the likelihood using the maximum value of the correlator for the first and second interferometers, and we have swept the third correlator vector in discrete steps (corresponding to the sampling rate of the detector) in order to maximize L.

In this way we have constructed a very simple likelihood function: all the terms concerning the "first" two detectors are constant, so its variations depend on the "third" correlator only.

For comparison we have reconstructed the source position with the coincident method too, using the time delays at which each correlator was maximum.

This first attempt was a rough test of the code for computing the likelihood. It has been useful to better understand the behavior of the correlator vectors as function of the arrival times.

6.5.1 The Monte Carlo

The data sets we have used for testing the strategy are the same used during the so-called LIGO-Virgo project 1b [2]. In that work, which aimed at comparing LIGO and Virgo analysis pipelines, 24 hours of data were used. The data consisted of simulated noise corresponding to the target sensitivity of the two LIGO 4km detectors and the Virgo detectors, and of simulated signals consisting of inspiral events, assumed to originate in the M87 galaxy ($\delta = 12°23', \phi = 187°41'$at 16 Mpc) and in the NGC6744 cluster ($\delta = -63°58', \phi = 286°23'$ at 10 Mpc), with polarization and orbit plane inclination chosen randomly from uniform distributions, and masses randomly selected from the set (1.0, 1.4, 2.0, 3.0 solar masses).

Since in that work the coincident method was used, the correlator vectors were not saved during the analysis. To make the present study possible, Leone Bosi has kindly re-analyzed the data sets using Distributed Signal Analyzer (better known as Merlino)

including the correlator at each interferometer around the maxima, with a 200 ms time window.

In the analysis our candidate events were defined by the presence of a double coincidence, corresponding to events having SNR$>$ 6 in two detectors. We have then considered all compatible events with at least SNR$>$ 4 in the third detector, so as to consider all possible triple coincidences, and we have then performed the analysis as detailed in 2.4.

6.5.2 Comparison of the results

As mentioned before, this first attempt to use the likelihood information was only the first test of the pipeline. We expected that maximize the likelihood over only one detector was not enough strong in determining the source position, with respect to a simple coincidence.

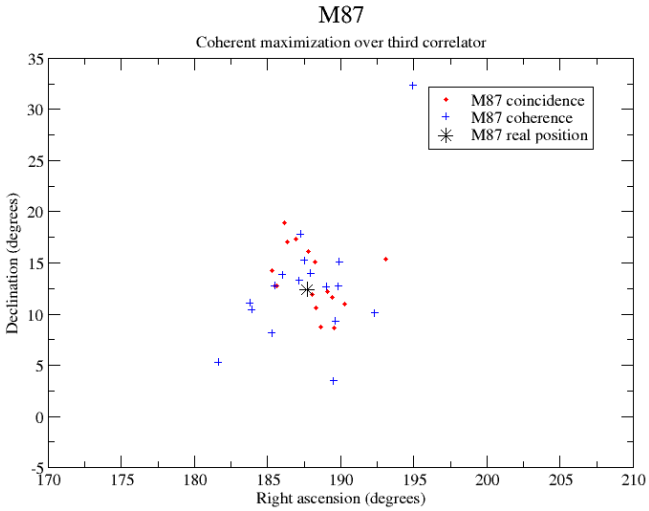

Figure 6.1:
M87 results

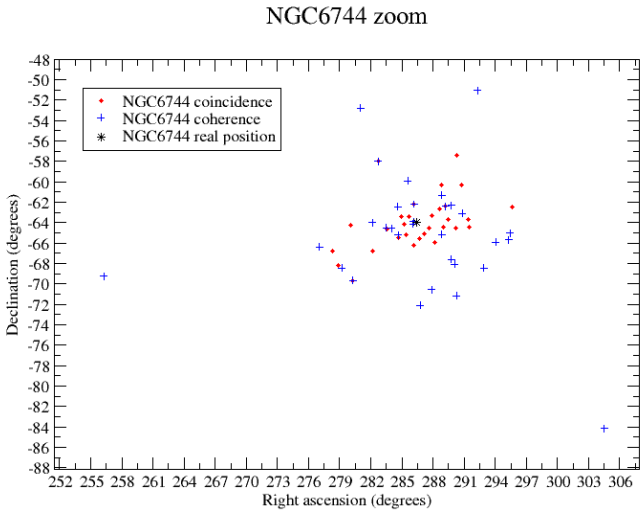

Figure 6.2:
NGC6744 results

From these plots we can see that this coherent and the coincident methods give similar results, but the coherent one does not seem to systematically improve the determination of the source position.

The results indeed told us that maximizing the likelihood just over one interferometer was not enough in order to appreciate a real coherent method, so we decided to perform the maximization over all the detectors.

Moreover, plotting the behavior of the likelihood as a function of the so called "third detector correlator" gave us the idea of fitting the likelihood over the three correlator vectors.

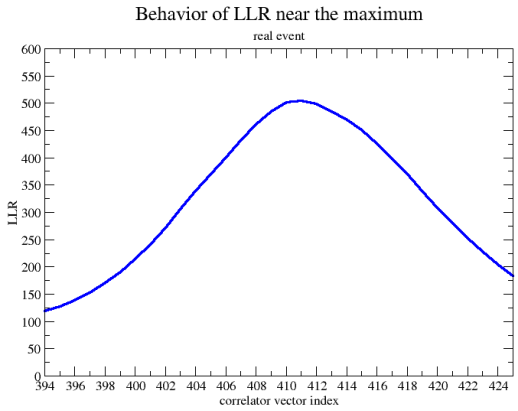

Figure 6.3:
The plot shows the behavior of the likelihood function for a real coincidence

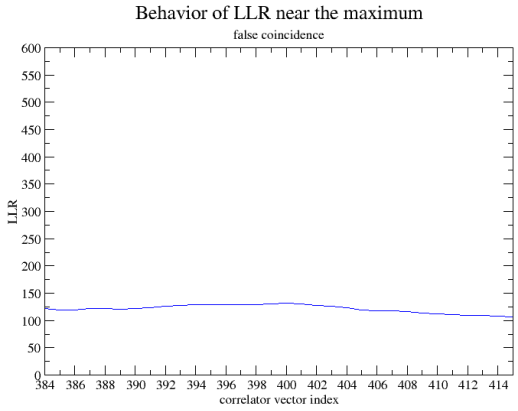

Figure 6.4:
The plot shows that in absence of a real coincidence, the LLR shape is quite flat.

6.6 An improvement of the method: coherent maximization and coherent fit

Trying to use as much as possible the likelihood information we have improved the method, performing a global maximization over all the correlator vectors simultaneously. We

have then computed the sky position using the time delays corresponding to the vectors elements that maximized the LLR.

In order to avoid the discretization due to the sampling rate and interpolate between them, we have performed also a "parabolic fit to the likelihood". Since the LLR is expected to display a maximum corresponding to the real position of the source, the idea is to fit its functional behavior around the maximum, instead of simply taking the measured maximum value. Consequently we have assumed that the likelihood could be fitted with a parabolic function of the correlators indexes:

$$A_1 (i - i_c)^2 + A_2 (j - j_c)^2 + A_3 (k - k_c)^2 +$$

$$+A_4 (i - i_c)(j - j_c) + A_5 (i - i_c)(k - k_c) A_6 (j - j_c)(k - k_c) +$$

$$+B_1 (i - i_c) + B_2 (j - j_c) + B_3 (k - k_c) + C \tag{6.22}$$

where i_c, j_c, k_c are the indexes corresponding to the maximum of each correlator.

We expected that the latter procedure should lead to a more precise reconstruction, since it makes use of all the data acquired around the maximum position. Moreover, the goodness of the fit, for instance by introducing a standard χ^2 test, could be used to discriminate false candidates.

Once the parabola was fitted on the data, the location of the vertex of the paraboloid was assumed as the reconstructed location for the candidate event: as a consequence of this maximization procedure, the reconstructed location did not correspond anymore to a set of time delays at the sampling positions used by each detector; the procedure effectively interpolated between samples and therefore potentially could have allowed to improve, for a sufficiently large SNR, the source location reconstruction, beyond the limits imposed by the finite sampling rates.

The coherent fit algorithm worked essentially as follow: first it computed the maximum of each correlator (actually of the function $\sqrt{C_0^{I\,2} + C_{\frac{\pi}{2}}^{I\,2}}$), and constructed around them a subset of each correlator vector. For example, if i is the correlator index and i_{max} the index of the maximum, a subset is made up of the correlator elements inside $[i_{max} - n,\, i_{max} + n]$. Then the algorithm calculates the likelihood for every triplet of correlator elements inside the range established, and successively fit it with the quadri-dimensional parabola.

We have tested the code with the data set described in par 3.1.1 and the results appeared quite good but the events were not enough in order to make a fair statistic (see paragraph 6.6.1).

Then we have produced a new dataset, enlarging the Monte Carlo (see paragraph 6.6.2), and actually the results we have found using this kind of coherent fit were not so promising: the coincident method and the coherent maximization were giving more accurate results in determining source position. After a lot of code cross-check we have

excluded that this negative result could be due to a bug. Instead, we believe it is due to an intrinsic limitation of the fitting procedure (see paragraph 6.9).

6.6.1 Comparison of the results

In order to make a comparison between the three methods, for each source we have plotted the three reconstructed positions:

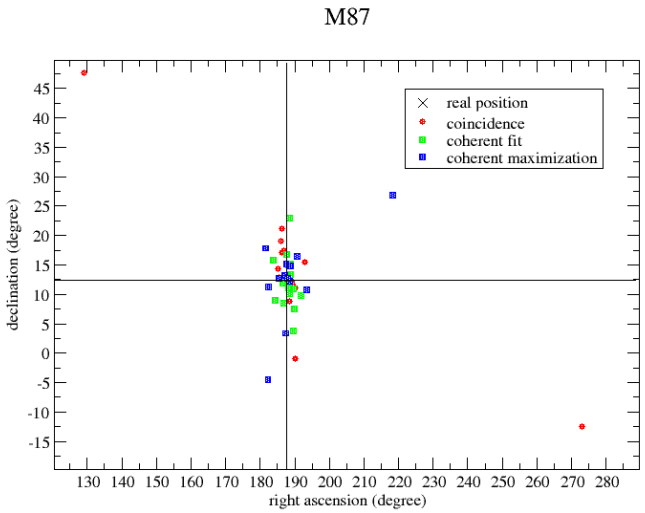

Figure 6.5:
M87 results

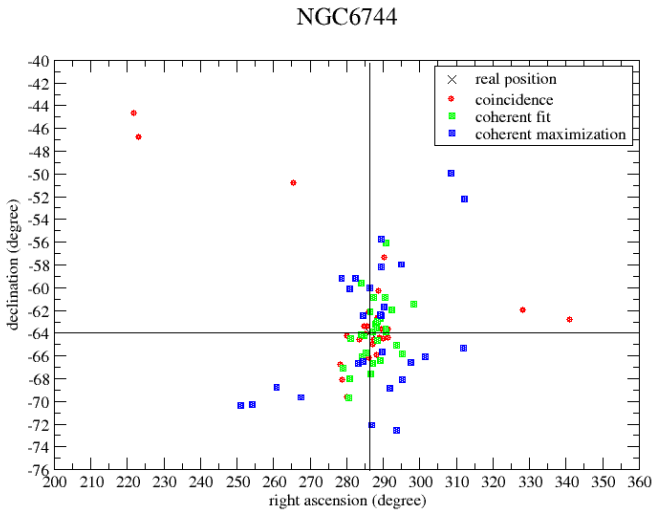

Figure 6.6:
NGC6744 results

The plots show that the "coherent fit" method seems the one that statistically gives the more precise position.

We can also characterize the accuracy in determining source position using a single angular parameter: the angular distance between the reconstructed position and the real one. This is useful also because we work with vectors and not with angles, so there are no singular points in the sky.

In order to make a more quantitative comparison, for each event we have plotted in a histogram the quantity:

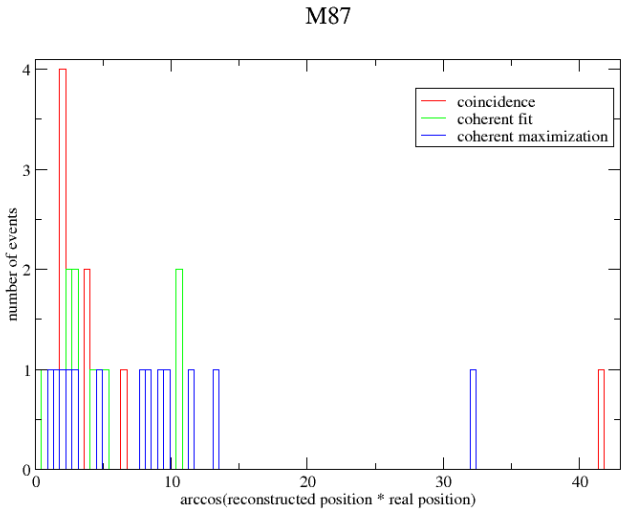

Figure 6.7:

- COINCIDENT arccos(reconstructed position · real position) Mean = 6°50′ Standard Deviation = 11°23′;
- COHERENT MAXIMIZATION arccos(reconstructed position · real position) Mean = 8°15′ Standard Deviation = 8°15′;
- COHERENT FIT arccos(reconstructed position·real position) Mean = 3°56′ Standard Deviation = 3°23′.

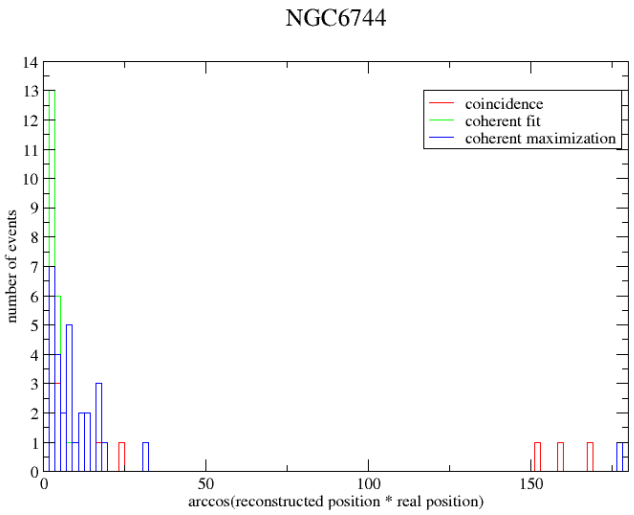

Figure 6.8:

- COINCIDENT arccos(reconstructed position · real position) Mean = 19°58′ Standard Deviation = 47°58′;
- COHERENT MAXIMIZATION arccos(reconstructed position · real position) Mean = 14°18′ Standard Deviation = 31°20′;
- COHERENT FIT arccos(reconstructed position·real position) Mean = 2°55′ Standard Deviation = 1°53′.

The simulated events coming from M87 were about 15, more or less half the number of the NGC6744's.

The huge value of standard deviation for the coincident analysis is due to the fact that there were a few events for which the coincident method failed altogether, while the two coherent methods have found reasonable positions. For that reason, these LIGO-Virgo simulated data were not enough to make a fair statistics, and to effectively test our method of analysis; we had to try a large number of sky positions, and with a much larger number of events per sky position in order to have reliable results.

6.6.2 The enlarged Monte Carlo

In our second step, since the number of events per sky position and the sky positions too were not enough to make a quantitative statistic, we have produced new data. For the new data sets we have used binary neutron stars (BNS) systems with $m_1 = m_2 = 1.45\,M_\odot$ and minimum gravitational frequency $f_0 = 30\,Hz$. With this choice, the signal duration is about 52 seconds.

For each sky location, signal are injected every about 100 s, at a distance of 1 Mpc, with polarization randomly distributed in $[-\pi, \pi]$ and inclination i uniformly distributed in $d\cos i$, that is $\cos i$ uniformly distributed in $[-1, 1]$.

Signal have been generated at 32 sky locations, in an equatorial reference frame fixed

with the Earth. In other words, the Earth has been kept non-rotating during the simulation, and the right ascension of the source corresponds to the celestial longitude in a reference frame for which stars at the zenith of Greenwich have zero right ascension.

The sky locations are the vertexes (20) and the centers of the faces (12) of a dodecahedron (it may be worth noticing that the 12 latter points constitute the vertexes of a icosahedron conjugated to the dodecahedron).

Two datasets have been produced, one at the nominal sampling rate of the detectors, the other at a reduced sampling rate. The nominal sampling rate are the same as those used for the LIGO-Virgo project 1b, that is 20 kHz for Virgo and 16384 Hz for LIGO detectors. For the other set, the sampling rate is 4 kHz for Virgo and 4096 Hz for LIGO detectors. For our analysis we have always used the dataset with reduced sampling rate, due to the prohibitive computational and time costs of the other. Naturally, in case of a real gravitational wave event, the analysis will (would) be performed at each detector nominal sampling rate.

In combining signals and noise, the signals have been scaled down to reasonable values of the SNR. To this end, we observe that the sight distance of Virgo, at SNR = 8, is about 32 Mpc (optimal) and 13 Mpc (averaged) for $1.45 - 1.45\,M_{\odot}$ binary neuron stars. Thus we have simulated events at 8 Mpc, 12 Mpc, 18 Mpc, 26 Mpc and 32 Mpc.

At this point, the data sets have been analyzed using 30 Hz as starting frequency and saving the correlator at each interferometer around the maxima, with a 8 ms time window.

In the analysis our candidate events were defined by the presence of a double coincidence, corresponding to events having SNR > 10 in two detectors. We have then considered all compatible events with at least SNR > 7 in the third detector, so as to consider all possible triple coincidences, and we have then performed the analysis.

6.7 The fit of each correlator

Trying to improve the accuracy of the reconstruction, we have performed a fit over each single correlator. Since very near to the event the correlator time series have a bell shape peaked at the event arrival time, we have constructed the function $\sqrt{{C_0^I}^2 + {C_{\frac{\pi}{2}}^I}^2}$ and fitted it with a parabola. This function, always positive, allows to merge the two quadratures information.

Thus, we have reprocessed the same data sets using this "improved" coincident method.

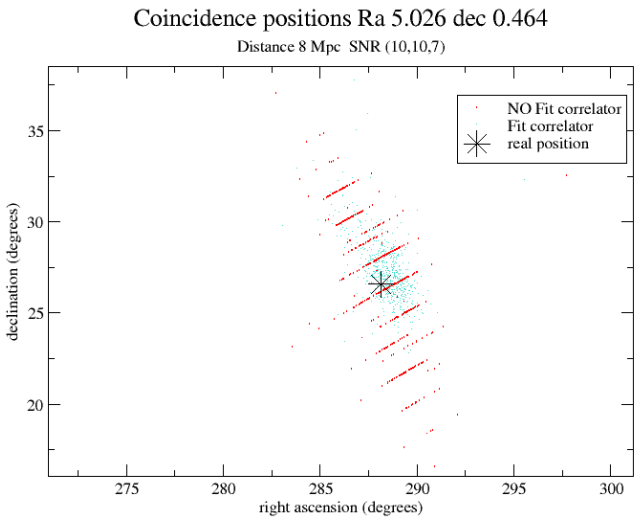

Figure 6.9:
The plot shows the results of the fit correlator procedure: the cian dots represents the reconstructed sky positions using the improved coincident method, while the red ones represents the positions founded by the old one.
The "comb" shape due to the finite sampling rate is disappeared making the fit of each correlator.

6.8 Searching for the best arrival time: End Time, Start Time or reference Time?

The coincident method for source position reconstruction works with detectors arrival times. The accuracy in determining the source position is limited by the precision in determining the time of arrival at each detector. The systematic uncertainties in this measurement are mainly due to the mismatch between the parameters of the real signal and the parameters of the template issuing the stronger trigger, among the templates used for matched filtering by each experiment. This causes a not perfect overlap between the template and true signal and consequently some timing errors. Furthermore, even when the template bank provides a very fine sampling of the parameter space, the detector noise causes random excursions across the template bank, as well as a statistical error on the arrival time.

Various choices are possible for the definition of the arrival time which is used for the triangulation. The matched filter corresponding to a certain individual template triggers at a time which corresponds to the signal "entering" the bandwidth of that template, at frequency ν_{min}. Since the arrival time is very sensitive to parameter mismatch between signal and template, the precision is better considering the so called "end time", which is obtained extracting the arrival time from the matched filtering procedure, and adding to it the duration of the triggering template. This determination is sensitive to the granularity of the template grid used for matched filtering. It has been shown [31] that the dependency on this granularity and the timing precision can be further improved by considering as

arrival time for the triangulation the one at which the signal crosses a reference frequency lying between ν_{min} and ν_{max}, and corresponding to a minimum of the detector sensitivity.

A little more in details, in doing the matched filtering procedure one finds how the template with the best overlap with the data stream should be shifted with respect to the true signal to get the best overlap between the two signals. This overlap is measured in terms of SNR, but since the SNR does not accumulate uniformly in the detector bandwidth, the matched filtering selects the template and the arrival time that give the best overlap with the signal in a frequency range important for the SNR. The phase difference between signal and template resulting in a timing error accumulates instead in the full frequency band. The idea that the authors showed in the [31] is to refer the timing to a reference frequency in the high SNR density region, in order to improve the resolution. This reference time is defined as follows:

$$t_{ref\,\nu_{ref}} = t_0 + T_{\nu_0 \to \nu_{ref}} \tag{6.23}$$

where t_0 is the time corresponding to the signal "entering" the bandwidth of that template, and $T_{\nu_0 \to \nu_{ref}}$ is the time necessary to the template signal to raise the reference frequency ν_{ref} starting from the frequency ν_0 .

We have first tested our codes by comparing the source position reconstruction using the end time and the reference time. The results are found in good agreement with [31]:

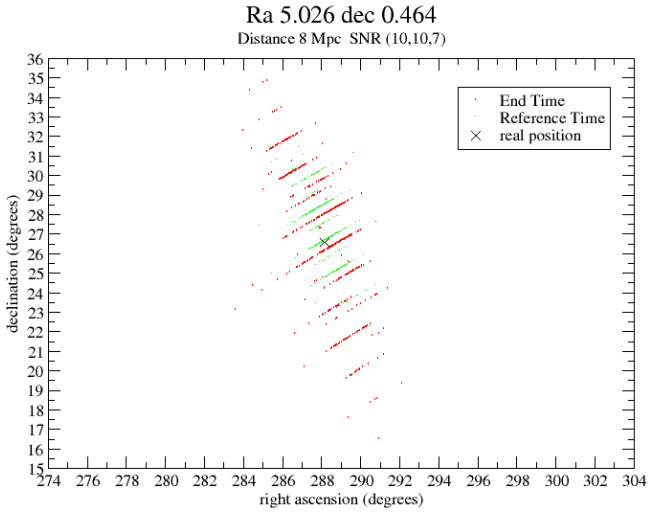

Figure 6.10:
From the plot we can see that using Reference Time in determining the source position (light green dots), we gain about a factor three.
If we take the angular distance α between the real position and the reconstructed one, and we compute its mean and standard deviation over the number of events, we obtain: for the End Time $\alpha_{mean} = 3°17'$and $\alpha_{std.dev} = 1°13'$, while for the Reference Time case, we have $\alpha_{mean} = 1°28'$ and $\alpha_{std.dev} = 2°13'$.

If we use the new powered coincident method using both Reference Time and fitting each correlator vector, the results are shown in the next plot:

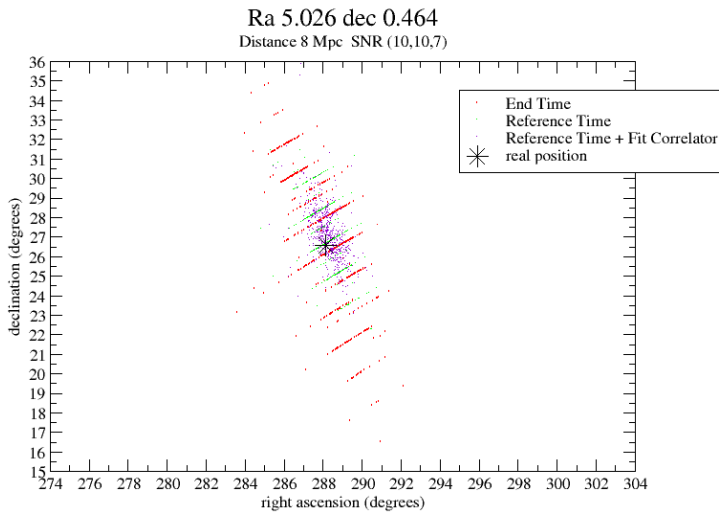

Figure 6.11:
In the plot the red dots represents the reconstructed position founded by the simple coincident method with end time, the light green dots represent the positions founded using reference time, and the purple dots represent the position founded by the "enhanced coincident method", for which the fit removes the sampling effect due to the finite sampling rate, and both the mean and standard deviation of the angular distance are slightly improved: $\alpha_{mean} = 1°21'$ $\alpha_{std.dev} = 1°59'$.

6.9 Coherent histogram

The coherent fit algorithm works essentially as follow:

First it computes the maximum of each correlator (actually of the function $\sqrt{C_0^{I\,2} + C_{\frac{\pi}{2}}^{I\,2}}$ for the reasons explained in 4.3), and constructs around them a subset of correlator vector. For example, if i is the correlator index and i_{max} the index of the maximum, a subset is made of correlator elements inside $[i_{max} - n, i_{max} + n]$. Then the algorithm calculates the likelihood (which is a real number) for every triplet of correlators elements inside the range established, and subsequently fits it with the quadri-dimensional parabola.

We have seen before that the results we have found using this kind of coherent fit were not so promising, and that we believe it is due to an intrinsic limitation of the fitting procedure. We will try to explain better this point.

Each correlator vector $C_0^I(t - \tau_I(\delta, \phi))$ is a function of two different times: where t is the "universal" arrival time of the event, for simplicity imagine that it is the time at which the gravitational wave reaches the centre of the earth, and it is obviously the same for all the interferometers. On the other hand $\tau_I(\delta, \phi)$ is the time delay of the $I - th$ detector with respect to the fide, and by definition different for each antenna: this difference allows to make the triangulation and determine the positions in the sky.

So, we have to maximize the likelihood with respect to these parameters separately, but the intrinsic accuracy of the two is very different and the algorithm for the coherent search does not take into account this fact. In other words, trying to fit the tri-dimensional

likelihood matrix using all its entries in this way is equivalent to not take into account the fact that we have two different and independent time parameters (actually four, the fide and each detector).

In terms of correlator vectors, when we construct the likelihood we vary the relative time delays between interferometers (and consequently we slowly modify the sky position) every time we make a step in any correlator. Every time each correlator makes one step so as to keep the same relative time delays between the detectors (and the sky position) we vary the fide arrival time.

As an alternative fitting procedure, when sweeping the correlators, we can produce a candidate sky position at each step so as to have the corresponding declination and right ascension for each value of the LLR. In this way we have the LLR as a direct function of declination and right ascension. In this way we can construct a sort of "histogram of the likelihood", which lives over a bi-dimensional grid of sky positions near the sky position resulting from the coincidence. The element ij-th on the grid is the largest LLR obtained for that bin in the sky positions. In this way we automatically maximize the likelihood over the fide arrival time, and then we proceed with the fit over the relative time delays.

This new object is a two-dimensional matrix, and represents the likelihood as a function of source declination and right ascension, maximized over the arrival time. Since the LLR is expected to display a maximum corresponding to the real position of the source, the idea of fitting its functional behavior around the maximum with a paraboloid is still reasonable.

So we have first plotted this histogram of the LLR for different events and for different sky position, obtaining very different and “complicated” shapes. Some examples are shown below.

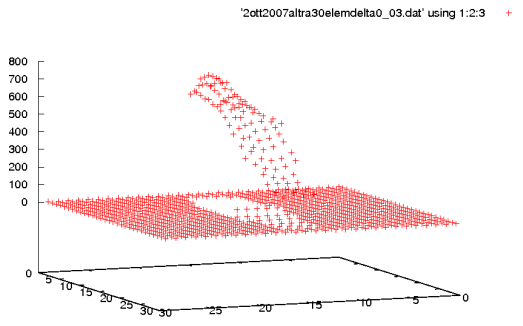

Figure 6.12:
Example of LLR shape

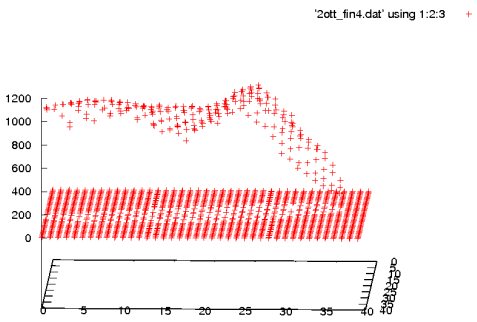

Figure 6.13:
Example of LLR shape

From these plots we have seen that the shapes of the LLR as function of the source position in the sky are too dis-homogeneous and complicated to be fitted with a reasonably simple analytic function.

6.10 The coherent weighted average

So we have tried to interpolate between samples computing the declination and right ascension weighted with their corresponding LLR value. More in details, once the LLR and its corresponding source position are computed, we select the ones that have angular distance from the position found with the optimized coincident method below 0.2 radians, and we use them to construct weighted averages.

6.10.1 Comparison of the results

The results are shown in the next plots, that represent the same sky position with events at different distances: 8, 12, 18 and 26 Mpc. Different thresholds have been applied for different source distances: for the 8 and 12 Mpc the threshold for a double coincidence is set at SNR 10, SNR 7 for the third interferometer; for the other distances the thresholds are SNR 6 and 5.

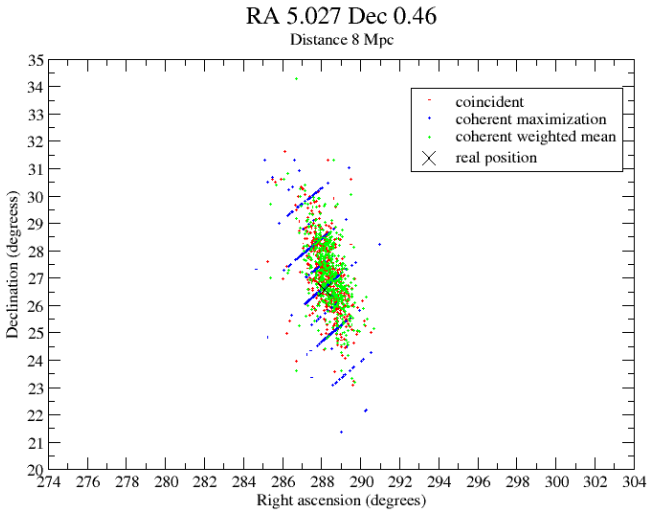

Figure 6.14:
Coincident arccos(reconstructed position · real position) Mean = 1°21′ Standard Deviation = 1°59′;
Coherent weighted average arccos(reconstructed position · real position) Mean = 1°22′ Standard Deviation = 1°59′.

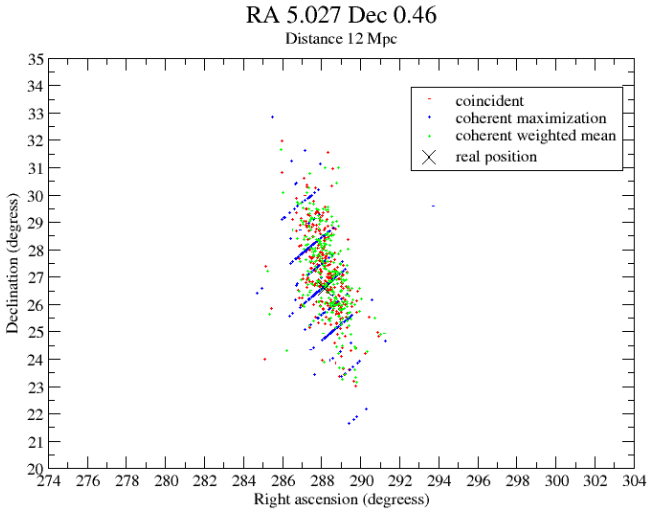

Figure 6.15:
Coincident arccos(reconstructed position · real position) Mean = 1°30′ Standard Deviation = 1°13′;
Coherent weighted average arccos(reconstructed position · real position) Mean = 1°30′ Standard Deviation = 1°10′.

For the next two distances, we have lowered the SNR threshold for the coincidences: SNR 6 for the double coincidence and 5 for the third detector, since otherwise the surviving events were not enough to make a “serious” statistic.

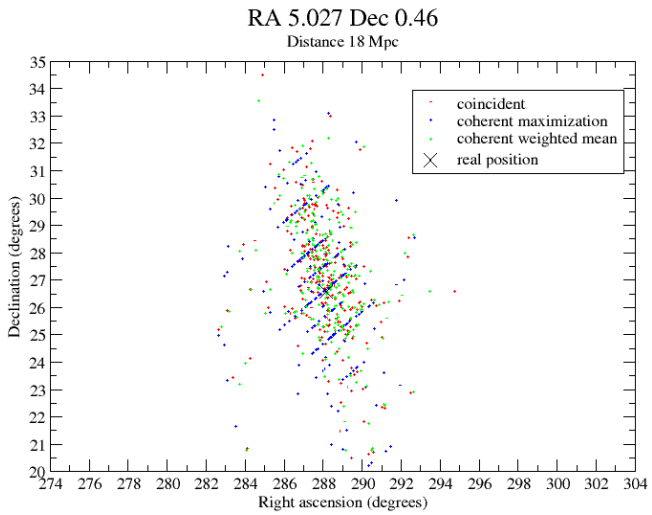

Figure 6.16:
Coincident arccos(reconstructed position · real position) Mean = 2°34′ Standard Deviation = 3°12′;
Coherent weighted average arccos(reconstructed position · real position) Mean = 2°31′ Standard Deviation = 3°08′.

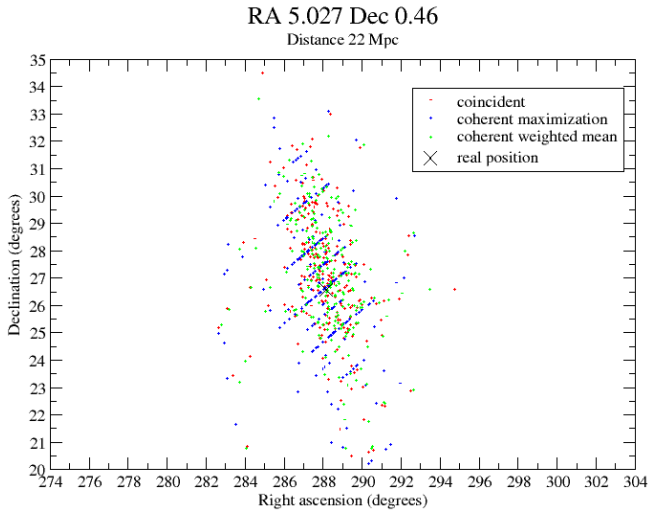

Figure 6.17:
Coincident arccos(reconstructed position · real position) Mean = 5°25′ Standard Deviation = 3°47′;
Coherent weighted average arccos(reconstructed position · real position) Mean = 5°15′ Standard Deviation = 3°38′.

Here we report a table with all the directions per source distance, in which we compare the angular distance α (in radians) computed with the enhanced coincident method and the coherent weighted average.

Decl	Right Asc	Coinc.mean α	Coinc.Std.Dev. α	Coher.mean α	Coher.Std.Dev.α
-1.570800	0.000000	0.024998	0.038433	0.082317	0.035186
-0.918438	0.000000	0.035236	0.056703	0.050142	0.053462
-0.918438	1.256640	0.021001	0.034017	0.024239	0.033451
-0.918438	2.513270	0.024796	0.052993	0.025116	0.053027
-0.918438	5.026546	0.054699	0.051774	0.052855	0.050883
-0.188711	0.000000	0.075864	0.077348	0.105511	0.069262
-0.188711	1.256640	0.027562	0.017702	0.024328	0.015506
-0.188711	2.513270	0.045140	0.032739	0.045571	0.030711
-0.188711	3.769915	0.041191	0.031738	0.047501	0.031523
-0.188711	5.026546	0.051210	0.027877	0.054621	0.026263
0.188711	3.141590	0.074896	0.062726	0.083242	0.065891
0.188711	4.398225	0.027270	0.035142	0.031080	0.034954
0.188711	5.654866	0.047702	0.032503	0.047154	0.031275
0.188711	0.628319	0.044700	0.029571	0.035757	0.023459
0.188711	1.884960	0.050090	0.036768	0.047489	0.031308
1.570800	3.141590	0.026584	0.046424	0.083038	0.040516
0.918438	3.141590	0.032737	0.022760	0.031382	0.021277
0.918438	4.398225	0.019591	0.029679	0.019980	0.029405
0.918438	5.654866	0.025214	0.047222	0.026657	0.046246
0.918438	1.884960	0.049679	0.042315	0.046589	0.040314
-0.463648	3.141590	0.041130	0.108147	0.039921	0.100181
-0.463648	4.398225	0.062688	0.050218	0.067917	0.049175
-0.463648	5.654866	0.139090	0.092551	0.170700	0.087687
-0.463648	0.628319	0.031336	0.021931	0.030726	0.021039
-0.463648	1.884960	0.024277	0.038496	0.022990	0.037329
0.463648	0.000000	0.029097	0.030496	0.058053	0.023940
0.463648	1.256640	0.052590	0.049798	0.047538	0.048505
0.463648	2.513270	0.128899	0.075516	0.175441	0.054762
0.463648	3.769915	0.029776	0.023453	0.030996	0.022441
0.463648	5.026546	0.023535	0.034806	0.023983	0.034706

Table 6.1: Mean angular distance between real source position and reconstructed one for the two methods of analyisis: the enhanced coincident one, and the coherent wheighted average one. Source distance: 8 Mpc

Decl	Right Asc	Coinc.mean α	Coinc.Std.Dev. α	Coher.mean α	Coher.Std.Dev.α
-1.570800	0.000000	0.029810	0.024482	0.084978	0.019349
-0.918438	0.000000	0.055199	0.035758	0.064048	0.027247
-0.918438	1.256640	0.028064	0.037229	0.029943	0.036807
-0.918438	2.513270	0.034708	0.072154	0.034464	0.072695
-0.918438	5.026546	0.077521	0.078549	0.075081	0.078571
-0.188711	0.000000	0.107614	0.079671	0.128623	0.074625
-0.188711	1.256640	0.033170	0.021026	0.029132	0.018782
-0.188711	2.513270	0.052782	0.034300	0.056149	0.030435
-0.188711	3.769915	0.047948	0.025679	0.051189	0.025485
0.188711	3.141590	0.062796	0.026130	0.070790	0.038321
0.188711	4.398225	0.033514	0.045711	0.036773	0.045284
0.188711	5.654866	0.047790	0.031267	0.045603	0.030605
0.188711	0.628319	0.053504	0.032204	0.044195	0.023815
1.570800	3.141590	0.031497	0.055160	0.086808	0.048765
0.918438	3.141590	0.042675	0.028176	0.041397	0.026365
0.918438	4.398225	0.022411	0.012267	0.023400	0.012472
0.918438	5.654866	0.030947	0.062908	0.031796	0.062400
0.918438	1.884960	0.055936	0.058481	0.052609	0.058042
-0.463648	3.141590	0.034453	0.029045	0.035443	0.028394
-0.463648	4.398225	0.064076	0.049742	0.065065	0.054430
-0.463648	0.628319	0.046575	0.032787	0.042851	0.029892
-0.463648	1.884960	0.026169	0.018135	0.024711	0.016705
0.463648	0.000000	0.038740	0.024720	0.063726	0.016956
0.463648	1.256640	0.061198	0.038284	0.052745	0.034313
0.463648	3.769915	0.053035	0.074258	0.053789	0.072209
0.463648	5.026546	0.026388	0.021259	0.026398	0.020466

Table 6.2: Mean angular distance between real source position and reconstructed one for the two methods of analyisis: the enhanced coincident one, and the coherent wheighted average one. Source distance: 12 Mpc

Decl	Right Asc	Coinc.mean α	Coinc.Std.Dev. α	Coher.mean α	Coher.Std.Dev.α
-1.570800	0.000000	0.048231	0.073973	0.098568	0.066885
-0.918438	0.000000	0.070354	0.053900	0.077127	0.046789
-0.918438	1.256640	0.056358	0.079915	0.057222	0.079695
-0.918438	2.513270	0.059622	0.118556	0.058258	0.118970
-0.918438	5.026546	0.112080	0.125863	0.108079	0.123564
-0.188711	0.000000	0.128029	0.123529	0.151833	0.115647
-0.188711	1.256640	0.052423	0.046381	0.048599	0.044364
-0.188711	2.513270	0.096003	0.136472	0.094734	0.128625
-0.188711	3.769915	0.069260	0.092318	0.068375	0.092114
0.188711	3.141590	0.098276	0.065828	0.108922	0.069475
0.188711	4.398225	0.056128	0.060673	0.057400	0.060322
0.188711	5.654866	0.061779	0.041188	0.056523	0.035706
0.188711	0.628319	0.075242	0.079369	0.067865	0.078289
0.188711	1.884960	0.012909	0.007447	0.011872	0.008768
1.570800	3.141590	0.053996	0.079551	0.103066	0.069516
0.918438	3.141590	0.059021	0.040073	0.057620	0.038280
0.918438	4.398225	0.050052	0.102424	0.051527	0.102414
0.918438	5.654866	0.049202	0.084640	0.049175	0.084884
0.918438	1.884960	0.073884	0.051253	0.070593	0.049062
-0.463648	3.141590	0.065316	0.109577	0.065323	0.110375
-0.463648	4.398225	0.092579	0.069117	0.086361	0.075959
-0.463648	0.628319	0.068430	0.034470	0.066184	0.036010
-0.463648	1.884960	0.049333	0.063154	0.046872	0.061950
0.463648	0.000000	0.054281	0.056874	0.076539	0.049712
0.463648	1.256640	0.062534	0.056374	0.063489	0.057251
0.463648	3.769915	0.056097	0.058717	0.060275	0.058074
0.463648	5.026546	0.044704	0.055902	0.044042	0.054945

Table 6.3: Mean angular distance between real source position and reconstructed one for the two methods of analyisis: the enhanced coincident one, and the coherent wheighted average one. Source distance: 18 Mpc

Decl	Right Asc	Coinc.mean α	Coinc.Std.Dev. α	Coher.mean α	Coher.Std.Dev.α
-1.570800	0.000000	0.064525	0.059408	0.108122	0.045952
-0.918438	0.000000	0.166977	0.033608	0.163093	0.032152
-0.918438	1.256640	0.068422	0.053275	0.070181	0.054229
-0.918438	2.513270	0.055158	0.050720	0.053111	0.048805
-0.188711	1.256640	0.073604	0.050421	0.068046	0.050114
-0.188711	3.769915	0.096413	0.037185	0.096254	0.033527
0.188711	4.398225	0.053162	0.036538	0.053007	0.034887
0.188711	0.628319	0.082230	0.043587	0.079643	0.043633
1.570800	3.141590	0.061366	0.048179	0.105286	0.035423
0.918438	3.141590	0.120255	0.101784	0.114912	0.098173
0.918438	4.398225	0.055508	0.067535	0.059319	0.064313
0.918438	5.654866	0.049482	0.043521	0.049647	0.041432
-0.463648	3.141590	0.090497	0.052466	0.089906	0.058726
-0.463648	1.884960	0.057469	0.066539	0.055963	0.064974
0.463648	0.000000	0.055998	0.032559	0.075776	0.027459
0.463648	5.026546	0.056016	0.049551	0.056280	0.048513

Table 6.4: Mean angular distance between real source position and reconstructed one for the two methods of analyisis: the enhanced coincident one, and the coherent wheighted average one. Source distance: 26 Mpc

Decl	Right Asc	Coinc.mean α	Coinc.Std.Dev. α	Coher.mean α	Coher.Std.Dev.α
-1.570800	0.000000	0.090337	0.115757	0.134286	0.099300
-0.918438	1.256640	0.055496	0.009137	0.060597	0.009004
-0.918438	2.513270	0.056555	0.028741	0.056150	0.026549
-0.188711	1.256640	0.095501	0.053618	0.083209	0.054427
0.188711	4.398225	0.059500	0.010751	0.060550	0.011989
1.570800	3.141590	0.063538	0.063238	0.111528	0.047505
0.918438	4.398225	0.037134	0.008948	0.047301	0.010056
0.918438	5.654866	0.064539	0.041762	0.064522	0.039033
-0.463648	1.884960	0.080793	0.048920	0.082217	0.050528
0.463648	5.026546	0.094464	0.066190	0.091621	0.063489

Table 6.5: Mean angular distance between real source position and reconstructed one for the two methods of analyisis: the enhanced coincident one, and the coherent wheighted average one. Source distance: 32 Mpc

6.11 What we have learned from this work

Our first purpose when we have started to work with coherent analysis was to use this method in order to refine the determination of the source position that we have reconstructed with a coincidence between three detectors. We first have searched for a coincidence, determining the arrival time at each detector, and reconstructing the source position using a triangulation. As a second step, like a successive order of approximation, we started to work more in details near to the gravitational waves event: using the correlator time series at each detector near to the event we have constructed the likelihood function, and worked in order to maximize it with respect to the detectors arrival times (and consequently, with respect to the source position in the sky). Making a "simple" maximization of the likelihood function, the accuracy with respect to the coincident method improved, but did not remove the effects of the finite sampling rate of the detectors, since if we plotted in a two-dimensional plot Right Ascension VS Declination, for each sky position the events did not form a "full ellipse" around the real position, but some regions in the ellipse seemed to be forbidden, and the resulting plot assumed a "lined" ellipse shape.

So we have slightly changed our aim: our priority became first of all to remove these forbidden regions due to the detectors finite sampling rate. The reconstructed locations corresponded indeed to a set of time delays in a certain way allowed by the sampling rate of the analysis of each detector, since the finite sampling rate implies necessarily a discretization of the possible detector arrival times, which is transmitted in the reconstructed source position. So we started to search for a new procedure which effectively interpolated between samples and therefore potentially could have allowed to improve, for a sufficiently large SNR, the source location reconstruction, beyond the limits imposed by the finite sampling rates.

Our first attempt was the most intuitive idea: fitting the likelihood function. Since the LLR is expected to display a maximum corresponding to the real position of the source, the idea was to fit its functional behavior around the maximum, instead of simply taking the measured maximum value. Unfortunately the results we have found were quite bad: the coincident method and the coherent maximization were giving more accurate results in determining source position.

After a lot of code cross-check we have excluded that this negative result could be due to a bug. But it resulted very important for another reason: during one of these several cross-checks we have tried how much the accuracy in reconstructing the source position was related with the definition of arrival time at each detector. Various choices are possible for the definition of the arrival time which is used for the triangulation: the classical is the so called "end time", but has been shown [31] that the timing precision can be further improved by considering as arrival time the one at which the signal crosses a reference frequency lying between ν_{min} and ν_{max}, and corresponding to a minimum of the detector sensitivity. We have first tested our codes by comparing the source position reconstruction using the end time and the reference time. The results were found not only in good

agreement with [31], but also in a very good agreement with the positions reconstructed using the coherent maximization of the likelihood: in terms of "lined ellipses" around the real position of the source, they could be almost overlapped, it means that using the reference time for making the coincidence, the accuracy in reconstructing the source position was essentially the same that the one found using the coherent maximization method. But the problem of the discretization of the portion of sky around the real position was not yet solved.

So we have tried to use the "coherent tools" as an improvement for the coincident method: during our cross-checks we have verified the shape of each correlator around an event, plotting it for each detector and for several source positions in the sky, and we have seen that every time the correlator time series could be fitted with a parabola. Fitting each correlator and using Reference Time we have seen an improvement with respect to the standard coincident procedure. The fit removes the sampling effect due to the finite sampling rate, and both the mean and standard deviation of the angular distance between the real and the reconstructed source positions resulted slightly improved. In a certain way, we have pushed the coincident method towards its limits, and we have crossed them using a "coherent instrument": the shape of each correlator time series, instead of simply their maxima.

The several code cross-checks resulted very helpful and precious for two different reasons: first of all they allowed the one that we call the "coherent code" to have a robust scientific validation, and also permitted to point out an intrinsic limitation of the coherent fit procedure (better explained in 6.8), which has been improved and refined. In a few words, instead of using the network statistic as a function of the arrival times at the three interferometers and try to fit it over them and simultaneously over a sort of "event time", independent from any detector position, we have verified that a better solution was to interpret the likelihood as a direct function of the two stellar coordinates in the sky. This allowed us to demonstrate, providing several examples that confirmed our intuitions: the likelihood assumes a more complicate shape with respect to the parabolic one, resulting actually quite impossible to fit in a simple way.

But this different interpretation of the likelihood values led us to a new idea for the coherent analysis, quite simple from the computational point of view: selecting an area in the sky close to the "coincident position" and reconstructing a coherent position taking the mean declination and right ascension weighted with their corresponding likelihood value. This new procedure resulted very efficient, since provides an accuracy consistent with the one obtained using the so called "enhanced coincident method" (obtained using the reference time and a fit of the shape of the individual correlator), and in a relatively automatic way.

The study of the accuracy problem, comparing the two methods of analysis gives in a certain way two important consequences: first of all the determination of the best coherent strategy for reconstructing the source position among all the alternatives, both in terms

of efficiency, and in terms of computational costs; and as a secondary effect it gives us the key for pushing the coincident method to its limits, provided that one uses all the correlators information.

From our results, we can infer that the arrival times dominate with respect to the wave amplitude in reconstructing the source position, since our improvements of the timing precision (using Reference Time and fitting each correlator) are substantially equivalent to the effect of the coherent analysis.

If we give a glance to the future, since new interferometric gravitational waves detectors are under construction and under project, another important feature of the coherent method is its flexibility to be adapted to a larger number of detectors. The coherent method can tell us how to combine them in order to obtain with the best accuracy the source position, instead of analyzing all the possible independent triangulations, and loosing in that way part of the event astrophysical information.

6.12 Future work: setting up the analysis pipeline

The successive step will be the inclusion of the code for the semi-coherent search in a Virgo network analysis pipeline. A possible scheme of the pipeline could be the following.

The data of each interferometer are separately analyzed in order to find the events, in particular characterized by the correlator vectors. This can be done with the standard Virgo pipelines (MBTA and Merlino), and with the LIGO inspiral pipeline for the two LIGOs. Successively the events output of these pipelines can be the input for the semi-coherent" method, which first of all will sweep the events searching for double coincidences in any pair of detectors. Then for each double coincidence, as better explained in 2.4, the code will search in the third interferometer correlator vector compatible events. For these events we have a triple coincidence, so, starting from the arrival time at each detector we can compute the network statistic over the three correlator vectors around that region and proceed with the position reconstruction.

According to the planned progress of the Virgo sensitivity, and of the draft agreement with the LIGO Scientific Collaboration, we expect that this coherent follow-up strategy will be tested using real LIGO and Virgo data.

Appendix A

Accuracy in the determination of source position as a function of the network area

In order to start a gravitational waves astronomy, there are under project new generation interferometers, so it is useful to analyze some solutions from the parameters estimation point of view. We have studied the coalescing binaries case, in particular the determination of source position in the sky using the coincidence analysis for networks of three detectors.

We have compared four different networks, in order to study the accuracy in determining the sky position as a function of the network area, and to try to quantify it.

So we have chosen four different networks:

- the first, composed by Virgo, GEO, and an hypothetical detector situated in the north-west of France which is the third vertex of a 1000 km side triangle, with a $5 \cdot 10^5 km^2$area;

- the second is a completely hypothetical network, "built" in order to maximize the network area inside Europe: an interferometer is in Sweden, one in Spain and the third in Sicily (approximate area of $5 \cdot 10^6 km^2$)

- the third is the "classic" Virgo-LIGO (the two 4 km LIGO at Hanford and Livingston), with an approximate area of $2 \cdot 10^7 km^2$;

- the last is composed by Virgo, an interferometer in Chile, at ESO site, and the other in Australia, at Perth (about $5 \cdot 10^7 km^2$area).

We have simulated events of twin neutron stars systems (1.4 solar masses) with maximum SNR 20 and setting a lower threshold at SNR 5. So we have generated 10^4 random sky positions (δ, ϕ), orbit inclinations respect to the line of sight (ϵ), and wave polarizations (ψ); for each of these events and for each interferometer, in order to simulate arrival times uncertainties, we have produced a Gaussian jitter of 10^3 time delays.

To estimate time delays variances we have used the empiric formula: $\sigma_{t_I} = 10^{-4} \frac{20}{SNR_I}$ where 20 is the best configuration SNR [1]:

$$SNR_{MAX} = 1.56 \cdot 10^{-19} \left(\frac{M_c}{M_\odot} \right)^{\frac{5}{6}} \frac{Mpc}{r} \sqrt{\int_0^{f_{max}} \frac{f^{-\frac{7}{3}}}{S_n(f)} df} \tag{24}$$

Its angular dependence can be computed using Gel'fand functions (for the definition of

Gel'fand functions see paragraph 2.3):

$$SNR_{ang}\left(\delta,\phi,\epsilon,\psi,\alpha_I,\beta_I,\gamma_I\right)=\sqrt{EBP^I\left(\delta,\phi,\epsilon,\psi,\alpha_I,\beta_I,\gamma_I\right)EBP^{I*}\left(\delta,\phi,\epsilon,\psi,\alpha_I,\beta_I,\gamma_I\right)}, \tag{25}$$

where $\alpha_I,\beta_I,\gamma_I$ are the Euler angles to transform coordinates expressed in the standard geocentric frame into coordinates expressed in the i-th detector frame, and EBP is the extended beam pattern function, defined as [1]:

$$EBP^I\left(\delta,\phi,\epsilon,\psi,\alpha_I,\beta_I,\gamma_I\right)=T_2^{2\,2}\left(\psi,\epsilon,0\right)D^I_{+2}\left(\delta,\phi,\alpha_I,\beta_I,\gamma_I\right)+T^{2\,2}_{-2}\left(\psi,\epsilon,0\right)D^I_{-2}\left(\delta,\phi,\alpha_I,\beta_I,\gamma_I\right) \tag{26}$$

and [1]

$$D^I_{\pm2}\left(\delta,\phi,\alpha_I,\beta_I,\gamma_I\right)=-i\,T^{2\,s}_{\pm2}\left(\phi,\delta,0\right)\left[T_s^{2\,2\,*}\left(\alpha_I,\beta_I,\gamma_I\right)-T_s^{2\,-2\,*}\left(\alpha_I,\beta_I,\gamma_I\right)\right] \tag{27}$$

where $s=\pm2$

We then have plotted these 10^4 variances in an histogram for the declination and for the right ascension, for all the networks, obtaining:

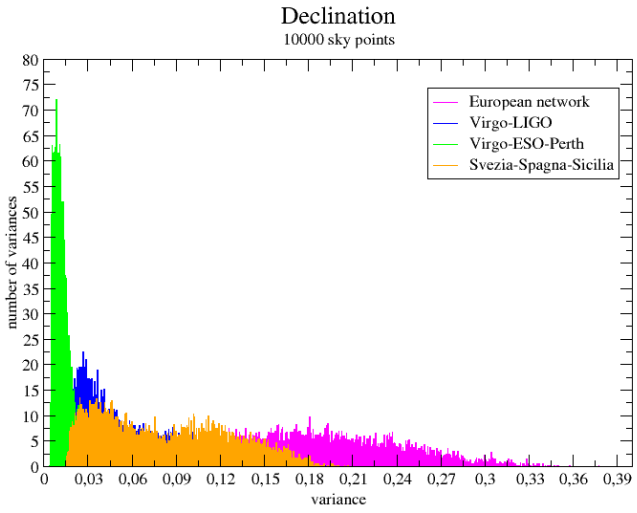

Figure 18:
Plot of the Declination accuracy for the different networks

As we can see the accuracy increases with the network area: for the smaller European network the mean variance is about 11 degrees, for the larger it decreases down to about 3 degrees, for the Virgo-LIGO ones is about 2 degrees, and for the intercontinental one is less then half a degree.

For the right ascension we have plotted the variance multiplied for the cosine of declination, in order to take into account the different radii of the celestial parallels, and the

result is quite similar to the declination one:

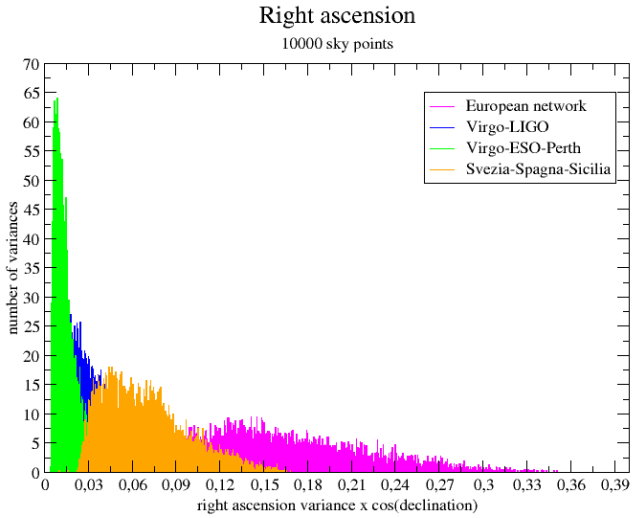

Figure 19:
Plot of the Right Ascension accuracy for the different networks

As for the declination, in the smaller European network case the mean variance is about 9 degrees, in the larger it reaches 2 degrees, in the Virgo-LIGO ones is about one degree, and in the Virgo-ESO-Perth ones is about half a degree.

Appendix B

Coalescing Binaries and Gamma Ray Bursts

Gamma Ray Bursts are intense flashes of γ and X ray, with duration from few milliseconds to several minutes, followed by a fainter emission at longer wavelengths, the so called afterglow. According to their duration, they are traditionally divided in short Gamma Ray Burst, lasting less then 2 s, that are associated with the final stage of the coalescence, the merging of the two stars; the other category are the so called long Gamma Ray Burts, whose progenitors are thought to be massive, low-metallicity stars exploding during collapse of their cores [35]. The sudden emission of a large amount of energy in a compact volume (of the order of tens km^3), leads to the formation of a relativistic fireball of e^+e^- pairs, γ rays and baryons that expand forming a jet, and part of the gravitational energy is emitted through gravitational waves. The electromagnetic emission originates in kinetic energy dissipation within the relativistic flow, and this phenomenon is supposed to take place at distances greater than $10^{13}cm$ from the source [35]. So the electromagnetic signal can give important information on the progenitor's nature, but indirectly, such as a constraint on the the structure and density of the circumstellar medium, which it allows the identification of host galaxies. As for the gravitational waves radiation, the energy radiated is located in the immediate neighborhood of the source, so an hypothetical observed gravitational waves signal would bring us direct information on the properties of the progenitor.

A common feature for long and short Gamma Ray Burts, is that the progenitors end as a rotating black hole with a massive disk of matter around it, whose accretion makes the ultra-relativistic fireball of the Gamma Ray Burst in the form of a jet, along the rotational axis of the system [35]. Due to the relativistic beaming effect, only observers located within the jet opening angle are able to observe the emission from the jet.

GRBs are detected at a rate of about one per day, from random directions in the sky [35]. In the last months some attempts to search for a gravitational waves coincidence with a Gamma Ray Burst have been done, more precisely for the GRB 050915a has been performed a search in coincidence with the Virgo detector [35], for the GRB030329 an attempt of coincidence with the LIGO detectors has been done [36]. Unfortunately, in both cases no gravitational events were found, but the studies results anyway very useful in the sense of detection strategy.

More recently has been studied the coincidence between the GRB 070201and LIGO [39], and some constraints for its astrophysical origin have been done. GRB 07201 was a short Gamma Ray Burst whose electromagnetically determined sky position is in the spiral arms of the Andromeda galaxy (M31), at a distance of about 770 kpc, with an isotropic energy release of about 10^{45} erg. At that the two LIGOs Hanford detectors were in data taking configuration, while the LIGO Livingston, GEO-600, and Virgo detectors were not taking data. First of all a search for gravitational waves from a compact binary inspiral has been performed, focusing on objects within the mass range $1\,M_\odot < M_1 < 3\,M_\odot$, $1\,M_\odot < M_2 < 40\,M_\odot$, since in order to generate a Gamma Ray Burst, at least one of the two objects has to be a "material" object, in other words a neutron star; the two spins has been ignored in constructing the template bank. The authors [39] have computed the likelihood of their observation, defined as the probability that no signal would be observed in the time of the GRB event duration, given the presence of a compact binary progenitor, varying the system parameters. Their results show that a compact binary progenitor for GRB 07201 has to be excluded at a confidence level beyond 99%. They have then tried to search for a gravitational wave burst associated with the GRB, using the cross correlation between the two detectors data-stream, after having them whitened, phase-calibrated and band- passed from 40 Hz to 2000 Hz. Such a model independent search did not find any burst event, and the authors set therefore an upper limit on the power emitted in gravitational waves by the GRB 07201, founding that it was probably less than $4.4 \cdot 10^{-4} M_\odot c^2$, corresponding to $7.9 \cdot 10^{50} ergs$.

Very recent improvements in the analysis techniques have been developed [37], and it could be a new tag for the forthcoming months.

GRB and gravitational waves sky maps: possible interactions?[2]

Swift is the currently NASA mission with international participation [40] whose aim is to detect and better understand Gamma Ray Bursts. The Swift telescope is composed by three instruments working together in order to provide rapid identification and multi-wavelength follow-up of Gamma Ray Bursts and their afterglows. Within 20 to 75 seconds of a detected GRB, the telescope provides the source location in the sky. The Burst Alert Telescope (BAT) works as first, it has an energy range of 15 - 150 keV (it is a γ ray detector), and a large field-of-view (2 steradians), which identifies burst positions with an accuracy of 4 arcmin ($0°04'$). Once the GRB is detected with the γ instrument, it is pointed by the X-ray Telescope (XRT), which has an energy range of 0.3 - 10 keV, and is able to obtain spectra of GRB afterglows during pointed follow-up observations. It has an higher accuracy position localizations, 5 arcs ($0°0'05''$). The last detector is an UV/Optical Telescope (UVOT), that takes images and obtains spectra of GRB afterglows. The images have an accuracy range of 0.3 - 2.5 arc-second, and the spectra are used to determine source distance through its redshift.

[2]Thanks a lot to Alessandra Corsi for her consulting and Gamma Ray Burst expertise.

From these details, one can easily infer that a current electromagnetic telescope is much more powerful with respect to a gravitational one (made up of a network of gravitational waves interferometers) in determining the source location in the sky. In this sense, a collaboration between electromagnetic and gravitational astronomers would be precious instead of making a gravitational waves full sky blind search, gravitational waves astronomers would search for an event in the position where a GRB has been detected. That kind of collaborations has already started, and will should continue in the forthcoming months, especially when the next generation of ground based gravitational waves interferometers will be taking scientific data.

However, an help from the gravitational wave astronomy in detecting new GRBs would come in all the cases of Gamma Ray Burst non-pointing towards the satellite location: in those cases the only chance to detect the GRB would be via its gravitational radiation.

Appendix C

The coherent network analysis for the other sources

The "coherent WaveBurst" method [34]

The so called "coherent WaveBurst" method combines the data streams of each detector in the network into a coherent statistic represented by the likelihood. With such an approach, the sensitivity of the network is not limited by the least sensitive detector in the network: the maximum likelihood ratio statistic represents indeed the total SNR of the signal detected in the network. Furthermore the method allowed to construct other coherent statistics, such as the null stream and the network correlation coefficient, in order to distinguish true gravitational waves signals from the environmental and instrumental false alarms. Finally, the source coordinates of the GW waveforms can be reconstructed, provided to use a network with at least three non-coincident interferometers.

In their work the authors have assumed Gaussian quasi-stationary noise, and have written the likelihood in the wavelet (time-frequency) domain:

$$LLR = \sum_{n=1}^{N} \sum_{i,j=1}^{K} \left(\frac{\omega_n^2[i,j]}{\sigma_n^2[i,j]} - \frac{(\omega_n[i,j] - F_{+n} h_+[i,j] - F_{\times n} h_\times[i,j])^2}{\sigma_n^2[i,j]} \right) \tag{28}$$

where N is the number of detectors in the network, $\omega_n[i,j]$ is the sampled detector data (time i and frequency j indexes run over some time-frequency area of size K), $\sigma_n[i,j]$ is the standard deviation of the detector noise, which may vary over the time-frequency plane, $F_{+n}(\theta,\phi)$ and $F_{\times n}(\theta,\phi)$ are the detector antenna patterns (depending on the source position) and $h_+[i,j]$, $h_\times[i,j]$ are the two polarizations of the gravitational wave signal in the wave frame. Since the detector responses are invariant with respect to the rotation around the z axis of the wave frame, the polarization angle is included in the definition of $h_+$and $h_\times$. The signal waveforms h_+ and $h_\times$ are found by variations of the likelihood.

They defined the data vector

$$\mathbf{w}[i,j] = \left(\frac{\omega_1[i,j]}{\sigma_1[i,j]}, ... \frac{\omega_N[i,j]}{\sigma_N[i,j]} \right) \tag{29}$$

and the antenna pattern vectors

$$\mathbf{f}_{+,\times}[i,j] = \left(\frac{F_{1+,\times}[i,j]}{\sigma_1[i,j]}, ... \frac{F_{N+,\times}[i,j]}{\sigma_N[i,j]} \right) \tag{30}$$

so as to write the maximum likelihood as

$$LLR_{max} = \sum_{\Omega_{tf}} \left[\frac{(\mathbf{w} \cdot \mathbf{f}_+)^2}{|\mathbf{f}_+|^2} + \frac{(\mathbf{w} \cdot \mathbf{f}_\times)^2}{|\mathbf{f}_\times|^2} \right] \tag{31}$$

The authors have introduced a so called likelihood regulator by changing the norm of the $\times$ polarization of the antenna pattern vector:

$$\left|\mathbf{f}'_\times\right|^2 = |\mathbf{f}_\times|^2 + \delta \tag{32}$$

where δ is a parameter whose value determines the strength of the constrain, for $\delta = 0$ one has the standard likelihood, and larger is δ, stronger is the constrain.

The resulting gravitational waves waveforms are:

$$h_+ = \frac{\mathbf{w} \cdot \mathbf{f}_+}{|\mathbf{f}_+|^2} \tag{33}$$

$$h_\times = \frac{\mathbf{w} \cdot \mathbf{f}_\times}{|\mathbf{f}'_\times|^2} \left[1 + \left(1 - \frac{|\mathbf{f}_+|^2}{|\mathbf{f}'_+|^2} \right)^{1/2} \right]^{-1} \tag{34}$$

where the second one strongly depend on the constrain δ.

For a given Time-Frequency location and point in the sky they defined

$$LLR_p(i,j,\theta,\phi) = |\mathbf{w}|^2 - |\mathbf{w} - \mathbf{f}_+\mathbf{h}_+ - \mathbf{f}_\times\mathbf{h}_\times|^2 \tag{35}$$

After the coherent triggers are identified, one has to reconstruct the parameters of the gravitational waves bursts associated with the triggers, such as the reconstruction of the source coordinates, the two wave polarizations, the individual detector responses and the maximum likelihood statistics of the triggers. The likelihood of reconstructed triggers is

$$LLR_c(\theta,\phi) = \sum_{i,j} LLR_p(i,j,\theta,\phi) \tag{36}$$

The maximum likelihood statistic LLR_m is obtained by variation of LLR_c over θ and ϕ. Unlike LLR_p, that is calculated for a single data sample, LLR_m is calculated simultaneously for all the data samples forming the coherent trigger.

These several coherent statistic constructed from the elements of the likelihood and null matrices, have been introduced by the authors in order to distinguish true burst signals from the instrumental and environmental glitches .

Ringraziamenti

Vorrei ringraziare il gruppo di Pisa che mi ha permesso di effettuare questo lavoro di tesi.

Un ringraziamento speciale va al mio relatore, Andrea, che mi ha aiutata ad arrivare fino qui e mi ha insegnato tantissime cose, lasciandomi peró "sbucciare le ginocchia" da sola, in modo che gradualmente imparassi a saper gestire la maggior parte dei problemi e delle situazioni in modo autonomo: non avrei potuto avere un relatore migliore, grazie davvero tanto!

Grazie anche a Leone, che ha pazientemente rianalizzato i dati del project 1b con Merlino in modo che io potessi svolgere la mia analisi e testare la procedura descritta nella Tesi.

Merci beaucoup á Frédérique, pour son aide, ses suggestions, ses conseils, et sa patience, merci mille fois!

Ringrazio tantissimo anche tutto il gruppo "coalescences" di Virgo, e tutti coloro, di Virgo e di EGO, che mi hanno accompagnata in questi tre anni di lavoro: grazie mille a tutti!!

Un grazie di cuore ai miei splendidi genitori, per esserci sempre stati quando ne avevo bisogno, per avermi incoraggiata nelle mie scelte, per tutto quello che mi hanno insegnato e trasmesso, per i loro preziosi consigli e suggerimenti, che spesso lí per lí non ascolto, ma che mi hanno sempre fatto riflettere e aiutata tanto, senza i quali non sarei sicuramente la persona che sono.

Grazie di cuore al mio fratellino, che mi ha sempre sostenuta, incoraggiata e consigliata, del quale sono e sono sempre stata fin da piccola orgogliosissima.

Un bacio a Carlo, perché spesso ha creduto in me e nelle mie capacitá piú di quanto ci abbia creduto io stessa, perché mi sta vicino e mi sostiene ogni giorno, perché mi ha migliorata tanto, perché fa di tutto per rendermi felice, perché é la persona piú meravigliosa che si possa avere accanto

Grazissimissime:

a Giulia, che anche se a distanza é sempre la mia "sorellina", e dopo questa definizione mi sembra che ogni altra parola sia superflua,

a Paola, che é un'amica veramente speciale e unica, con la quale ci siamo "addomesticate" a vicenda negli anni, e con la quale ho condiviso i momenti di stress pre-laurea, il periodo dei concorsi di dottorato, la ricerca di post-doc, e un sacco di altre cose,

a Manu, perché anche se ci sentiamo di rado e siamo lontane, il nostro bellissimo

rapporto di amicizia é rimasto come ai tempi di laboratorio 3 insieme e della vacanza a Parigi con Sara,

a Diego, perché é un amico carissimo come ce ne sono pochi, su cui sono sempre stata sicura di poter contare,

a Filippo, perché da quando ci conosciamo dal primo anno di Universitá "ci sopportiamo" e siamo carissimi amici nonostante i caratteri diversi, e perché c'é sempre nei momenti del bisogno,

a France, perché é una carissima amica, siamo cresciute insieme e ne abbiamo fatta di strada da quella volta in cui lei e Emily si litigavano perché tutte e due volevano montare sui batti-batti con me, il giorno in cui ci siamo conosciute,

a Emily, perché é una carissima amica, per le nostre lunghe chiacchierate e passeggiate sul mare importantissime per "ricaricarsi" dopo giorni e giorni di lavoro, perché siamo riuscite a rimanere unite e in contatto in tutti questi anni,

a Giorgio, che é mio amico da quando doveva decidere quale scuola superiore scegliere, e me lo raccontava facendo il riscaldamento al campo scuola, per gli anni in cui siamo stati compagni di Universitá, e anche per avermi "costretta", insieme a Filippo, ad andare all'ennesimo compitino di fisica1 quando ero scoraggiata, proprio la volta in cui avrei finalmente passato l'esame; e grazie per esserci ancora,

a Marina, carissima compagna di ufficio e di chiacchierate, che sopporta pazientemente le mie "uscite strane" tipo quella sul cane nella presentazione, (o peggio a Potsdam..) e nonostante queste é una mia cara amica,

a Maddalena, la mia prima compagna di ufficio a Virgo, compagna di momenti stress, che abbiamo sopportato anche grazie alle pause-chiacchierate, durante le quali é cresciuta la nostra amicizia

a Marco, caro amico e compagno di pranzi-battibecchi e lunghe chiacchierate sugli argomenti piú disparati,

a Ale, il mio "gemello", con il quale sono cresciuta insieme correndo al campo scuola, e perché c'é ed é un amico carissimo anche ora dopo anni che non corriamo piú,

a Domenico, per esserci sempre anche se ci sentiamo poco,

a Elisabetta, a Matteo, a Enrico, Gabriele, per essere amici oltre che compagni di lavoro,

al mio allenatore, che anche se non corro piú ormai da anni, é sempre "il mio allenatore",

a Lucia e Claudina, che ho conosciuto da poco ma che sono amiche davvero care, e sono stata proprio fortunata ad averle trovate,

a tutti gli altri che mi hanno "accompagnata" fino qui, grazie mille, davvero!

Bibliography

[1] A. Pai, S. Dhurandhar, S. Bose "Data-analysis strategy for detecting gravitational-wave signals from inspiraling compact binaries with a network of laser-interferometric detectors", Phys. Rev. D 64, 042004 (2001)

[2] F. Beauville, M.-A. Bizouard, L.Blackburn, L. Bosi, L. Brocco, D. Brown, D. Buskulic, F. Cavalier, S. Chatterji, N. Christensen, A.-C. Clapson, S. Fairhurst, D. Grosjean, G. Guidi, P. Hello, S. Heng, M. Hewitson, E. Katsavounidis, S. Klimenko, M. Knight, A. Lazzarini, N. Leroy, F. Marion, J. Markowitz, C. Melachrinos, B. Mours, F. Ricci, A. Viceré, I. Yakushin, M. Zanolin "Detailed comparison of LIGO and Virgo Inspiral Pipelines in Preparation of a Joint Search", Class. Quantum Grav. 25 045001 (2008).

[3] Astone P., Babusci D., Baggio L., Bassan M., Blair D. G., Bonaldi M., Bonifazi P., Busby D., Carelli P., Cerdonio M., Coccia E., Conti L., Cosmelli C., D'Antonio S., Fafone V., Falferi P., Fortini P., Frasca S., Giordano G., Hamilton W. O., Heng I. S., Ivanov E. N., Johnson W. W., Marini A., Mauceli E., McHugh M. P., Mezzena R., Minenkov Y., Modena I., Modestino G., Moleti A., Ortolan A., Pallottino G. V., Pizzella G., Prodi G. A., Quintieri L., Rocchi A., Rocco E., Ronga F., Salemi F., Santostasi G., Taffarello L., Terenzi R., Tobar M. E., Torrioli G., Vedovato G., Vinante A., Visco M., Vitale S., Zendri J. P., "Methods and result of the IGEC search for burst gravitational waves in the years 1997-2000", Phys. Rev. D 68, 02201 (2003).

[4] Belczynski K., Kalogera V., Bulik T., "A comprehensive study of binary compact objects as gravitational wave sources: evolutionary channel, rates, and physical properties", Astrophys. J. 572 (2001) 407-431.

[5] Blanchet L., "Energy loss by gravitational radiation in inspiraling compact binaries to 5/2 post-Newtonian order", Phys. Rev. D 54, 1417 (1996).

[6] Culter C., Flanagan E. E., "Gravitational waves from merging compact binaries: How accurately can one extract the binary's parameters from the inspiral waveform?", Phys. Rev. D 49 2658 (1993).

[7] Fabri E., "Argomenti di Cosmologia e Astrofisica Relativistica", Anno Accademico 2001-02, ftp://osiris.df.unipi.it/pub/sagredo/afrel

[8] Hurley J. R., Tout C. A., Pols O. R., "Evolution of Binary Stars and the Effects of Tides on Binary Populations", Mon. Not. R. Astron. Soc. 000, 1-36 (2000).

[9] Nutzman P., Kalogera V., Finn L. S., Hendrickson C., Belczynski K., "Gravitational Waves from Extragalactic Inspiraling Binaries: Selection Effects and Expected Detection Rates", astro-ph/0402091 v2 (2004).

[10] Owen B. J., Sathyaprakash B. S., "Matched filtering of gravitational waves from inspiraling compact binaries: Computational cost and template placement", Phys. Rev. D 60, 022002 (1999).

[11] Owen B. J., "Search templates for gravitational waves from inspiraling binaries: Choice of template spacing", Phys. Rev. D 53, 6749-6761 (1996).

[12] Viceré A., "Network analysis for coalescing binaries: coherent versus coincidence based strategies", Class. Quantum Grav. 21 (2004)

[13] P.Jaranowski, A. Krolak, "Optimal solution to the inverse problem for the gravitational wave signal of a coalescing compact binary", Phys. Rev D 49,1723 (1994)

[14] Paolicchi P., "Lezioni di Astrofisica II", http://www.df.unipi.it/~paolic/dispense.html .

[15] Castellani V., "Astrofisica stellare - I fondamenti fisici dell'interpretazione evolutiva di stelle e galassie", Ed. Zanichelli, Bologna (1985).

[16] Benacquista M. J., "Relativistic Binaries in Globular Clusters", Living Rev. Rel. 5 (2002) 2, http://relativity.livingreviews.org/lrr-2002-2 (2002).

[17] Schutz B. F. "Gravitational-wave sources", Class.QuantumGrav. 13 A219-A238 (1996).

[18] Losurdo G., "Ultra fequency Inverted Pendulum for the VIRGO Test Mass Suspension", Tesi di Perfezionamento in Fisica, Scuola Normale Superiore di Pisa (1998)

[19] Saulson P. R., "Fundamentals of interferometric gravitational wave detectors", World Scientific Publishing Co., Singapore (1994)

[20] N. Stergioulas, "Rotating Stars in Relativity", Living Rev. Relativity 6, (2003), 3. URL (cited on <15 November 2007>): http://www.livingreviews.org/lrr-2003-3

[21] A. Viceré "Introduction to the data analysis in interferometric gravitational wave experiments" , World Scientific, inside the "Experimental physics of gravitational waves", Proceedings of the International Summer School Urbino, Italy 6 - 18 September 1999

[22] F. Marion et al (the Virgo Collaboration) "Multi-band search of coalescing binaries applied to Virgo CITF data", 2004 Gravitational waves and experimental gravity Proc. Rencontres de Moriond 2003

[23] J. H. Taylor, J. M. Weiseberg "A new test of General Relativity: gravitational radiation and the binary pulsar PSR 1913+16", 1982 The Astrophysical journal 253: 908-920

[24] S. Bonazzola, E, Gourgoulhon "Gravitational waves from pulsars: emission by magnetic-field-induced distortion", 1996 Astronomy and Astrophysics 312, 675-690

[25] M. Maggiore, "stochastic background of gravitational waves", Lecture given at the: Gravitational Waves: A Challenge to Theoretical Astrophysics. Trieste, 5-9 June 2000, arXiv:gr-qc/0008027v1

[26] T. Regimbau, B. Chauvineau, "Stochastic background from extra-galactic double neutron stars", arXiv:0707.4327v1 [gr-qc] ,2007.

[27] T. Regimbau, J. A. de Freitas Pacheco, "Stochastic Background from Coalescences of NS-NS Binaries", arXiv:gr-qc/0512008v2, 2006

[28] L. Bosi et al (the Virgo Collaboration), "Search for inspiralling binary events in the Virgo Engineering Run data", Class. Quantum Grav. 21 (2004) S709-S716

[29] L. Bosi et al (the Virgo Colaboration), "A parallel in-time analysis system for Virgo", Journal of Physics: Conference series 32 (2006) 35-43, Sixth Edoardo Amaldi Conference on Gravitational Waves

[30] M. Mantovani, "The Automatic Alignment in the Virgo interferometer", PhD Thesis in Experimental Physics, UniversitÃă degli Studi di Siena, 2007.

[31] D. Grosjean et al (the Virgo Collaboration), "Improving the timing precision for inspiral signals found by interferometric gravitational wave detectors", Class. Quantum Grav. 24 (2007) S617-S625

[32] J. A. de Freitas Pacheco, T. Regimbau, S. Vincent and A. Spallicci, "Expected coalescence rates of NS-NS binaries for laser beam interferometers", arXiv:astro-ph/0510727v1, 2005

[33] F. Mannucci, D. Maoz, K. Sharon, M. T. Botticella, M. Della Valle, A. Gal-Yam, and N. Panagia, "The supernova rate in local galaxy clusters", arXiv:0710.1094v1 [astro-ph], 2007

[34] S. Klimenko, I. Yakushin, A. Mercer, G. Mitselmakher, "Coherent method for detection of gravitational wave bursts ", arXiv:0802.3232v2 [gr-qc], 2008

[35] A. Corsi and the Virgo Collaboration, "Search for gravitational waves associated with GRB 050915a using the Virgo detector ", arXiv:0803.0376v1 [gr-qc], 2008

[36] The LIGO Scientific Collaboration, "A Search for GravitationalWaves Associated with the Gamma Ray Burst GRB030329 Using the LIGO Detectors", arXiv:gr-qc/0501068v3, 2005

[37] The LIGO Scientific Collaboration, "GRB-triggered searches for gravitational waves in LIGO data", arXiv:0802.0393v1 [gr-qc], 2008.

[38] M. Punturo, "Advanced Virgo Sensitivity Curve: a possible scenario", VIR-NOT-PER-1390-283 (2004).

[39] The LIGO Scientific Collaboration, "Implications for the origin of GRB 070201 from LIGO observations", arXiv:0711.1163v2 [astro-ph] 28 Nov 2007

[40] http://heasarc.gsfc.nasa.gov/docs/swift/swiftsc.html